Correlating the Structural Evolution of ZnO/Al_2O_3 to Spinel Zinc Aluminate with its Catalytic Performance in Propane Dehydrogenation

Manouchehr Nadjafi, [†] *Agnieszka M. Kierzkowska,*[†] *Andac Armutlulu,*[†] *Rene Verel,*[§] *Alexey Fedorov,*[†]
Paula M. Abdala,[*†] *and Christoph R. Müller*[*†]

† Laboratory of Energy Science and Engineering, Department of Mechanical and Process Engineering, ETH Zürich, CH-8092, Zürich, Switzerland

§ Laboratory of Inorganic Chemistry, Department of Chemistry and Applied Biosciences, ETH Zürich, CH-8093, Zürich, Switzerland

ABSTRACT: Zn-based Al_2O_3-suported materials have been proposed as inexpensive and environmentally friendly catalysts for the direct dehydrogenation of propane (PDH), however, our understanding of these catalysts' structure and deactivation routes is still limited. Here, we correlate the catalytic activity for PDH of a series of Zn-based Al_2O_3 catalysts with their structure and structural evolution. To this end, three model catalysts are investigated. (i) ZnO/Al_2O_3 prepared by atomic layer deposition (ALD) of ZnO onto γ-Al_2O_3 followed by calcination at 700 °C, which yields a core-shell spinel zinc aluminate/γ-Al_2O_3 structure. (ii) Zinc aluminate spinel nanoparticles ($Zn_xAl_yO_4$ NPs) prepared via a hydrothermal method. (iii) A reference core-shell ZnO/SiO_2 catalyst prepared by ALD of ZnO on SiO_2. The catalysts are characterized in detail by synchrotron X-ray powder diffraction (XRD), Zn K-edge X-ray absorption spectroscopy (XAS), and ^{27}Al solid state nuclear magnetic resonance (ssNMR). These experiments allowed us to identify tetrahedral Zn sites in close proximity to Al sites of a zinc aluminate spinel phase (Zn_{IV}–O–$Al_{IV/VI}$ linkages) as notably more active and selective in PDH relative to the supported ZnO wurtzite phase (Zn_{IV}–O– Zn_{IV} linkages) in ZnO/SiO_2. The best performing catalyst, $50ZnO/Al_2O_3$ gives 77% selectivity to propene (gaseous products based) at 9 mmol C_3H_6 g_{cat}^{-1} h^{-1} space time yield (STY) after 3 min of reaction at 600 °C. On the other hand, the core-shell ZnO/Al_2O_3 catalyst shows an irreversible loss of activity over repeated PDH and air-regeneration cycles, explained by Zn depletion on the surface due to its diffusion into subsurface layers or the bulk. $Zn_xAl_yO_4$ NPs gave a comparable initial selectivity and catalytic activity as $50ZnO/Al_2O_3$. With time on stream, $Zn_xAl_yO_4$ NPs deactivate due to the formation of coke at the catalyst surface, yet the extend of coke deposition is lower than for the ZnO/Al_2O_3 catalysts, and the activity of $Zn_xAl_yO_4$ NPs can be regenerated almost fully using calcination in air.

1. INTRODUCTION

Propene is a key commodity for the production of a wide variety of chemicals such as polypropylene, propene oxide, acrylonitrile, cumene or acrylic acid.[1] Currently, the supply of propene from traditional routes such as fluid catalytic cracking (FCC) and steam cracking of naphtha[2] is reducing due to the replacement of naphtha by ethane in crackers (owing to the availability of inexpensive shale gas).[3] The main industrial on-purpose technologies for the dehydrogenation of propane to propene (PDH) are the Catofin^{TM} and the Oleflex^{TM} processes that rely on Cr- and Pt-based catalysts, respectively.[4] [2] However, due to the high price and low availability of platinum and the toxicity of Cr^{VI},[5] the development of alternative, low cost and environmentally benign catalysts is of great importance.[6]

Metal oxide catalysts, including gallium, cobalt, aluminum and zinc oxide-based catalysts, are currently researched actively for the selective dehydrogenation of propane to propene.[2, 7-13] The metal sites on the surface of these oxides can exhibit different coordination environments and undergo changes in the oxidation state during the PDH reaction, which affect their catalytic performance. This has driven considerable research efforts to understand the active sites at the atomic level.[9, 14-17] Catalysts with active Zn sites (primarily, dispersed Zn^{2+} cations or complex oxides containing Zn^{2+}, for instance spinel-type oxides or zeolites) are promising candidates considering the low cost and generally low toxicity of Zn.[9, 18] Bulk ZnO is considered almost inactive in PDH.[14] The low activity of ZnO is worsened by the instability of bulk ZnO in reducing conditions at high temperatures (>550 °C), i.e., ZnO can reduce to metallic Zn (melting point of Zn is 420 °C) and/or form volatile Zn species.[14, 19] However, it has been reported that the most active and selective Zn-based alkane dehydrogenation catalysts contain dispersed Zn^{2+} cations stabilized on a support.[8, 9, 14, 19, 20] Several studies suggest that the nature of the support determines the local structure and coordination geometry of the Zn sites and therefore influences the catalyst's performance.[9, 21] That being said, the atomic scale structure of the most active sites in Zn-containing catalysts remains under intensive investigation. For example, isolated Zn^{2+} cations with tetrahedral coordination have been proposed as active sites for alkane dehydrogenation in Zn-containing zeolites.[20, 22, 23] In addition, it has been suggested that the proximity of Zn^{2+} and Al^{3+} sites plays an important role, as basic Al-bound oxygen is essential for the heterolytic cleavage of the C−H bond, according to theoretical calculations.[7, 18] The active sites in alumina supported zinc-based catalysts, prepared by wetness impregnation (WI) or chemical vapor deposition

(CVD), were assessed by temperature programmed reduction (TPR) and diffuse reflectance infrared Fourier transform spectroscopy (DRIFT) with probe molecules (CO, H_2) and Zn^{2+} sites bonded to alumina were reported to be the active sites with much higher reducibility compared to supported ZnO nanoparticles.[8] Moreover, single site Zn^{2+} on silica support[14, 21] and more recently, tricoordinated isolated Zn^{2+} sites anchored on (doped) ZrO_2 were also reported to be highly active in PDH.[2, 9] While such dispersed Zn^{2+} sites are highly active, they can be reduced during the PDH leading to catalyst deactivation with time on stream (TOS). Other deactivation routes of Zn^{2+} sites include coke deposition, ZnO formation or Zn difussion,[8 18] whereby in particular the latter process deserves further detailed structural studies.

In this work, we aim at: i) describing the nature of Zn sites in ZnO layers supported on γ-Al_2O_3 (denoted 10, 30, and 50ZnO/Al_2O_3) obtained by atomic layer deposition, ii) understanding the interplay between the coordination of Zn and Al sites, their local structure, and the catalytic activity in PDH, and iii) determining deactivation routes. We address these scientific questions by evaluating in detail the atomic scale structure and catalytic performance for ZnO/Al_2O_3 and ZnO/SiO_2 model catalysts prepared via ALD of ZnO on γ-Al_2O_3 or SiO_2, respectively, followed by a heat treatment at 700°C. Further, we synthesize $Zn_xAl_yO_4$ nanoparticles (NPs, ca. 4 nm average crystallite size) using a hydrothermal approach. We investigate the structure of these catalysts via synchrotron X-ray powder diffraction (XRD), X-ray absorption spectroscopy (XAS) at the Zn K-edge, ^{27}Al solid-state nuclear magnetic resonance (ssNMR), and transmission electron microscopy (STEM). Our findings show that upon thermal treatment, ALD-deposited ZnO reacts with γ-Al_2O_3, yielding tetrahedral Zn^{2+} in a zinc aluminate phase shell that covers the γ-Al_2O_3 core. The Zn_{IV}–O–$Al_{IV/VI}$ linkages present in ZnO/Al_2O_3 outperform poorly active Zn_{IV}-O-Zn_{IV} linkages found in ZnO/SiO_2 in terms of PDH catalytic activity and selectivity. However, ALD-derived, core-shell ZnO/Al_2O_3 catalysts deactivate significantly with TOS and over repeated air regeneration cycles. We explain this deactivation by the diffusion of Zn from the surface layers into the inner layers of alumina, leading to an irreversible loss of activity. The initial space-time yield (STY, per gram of catalyst) of $Zn_xAl_yO_4$ NPs was similar to that of ZnO/Al_2O_3; both materials contain Zn_{IV}-O-$Al_{IV/VI}$ sites. $Zn_xAl_yO_4$ NPs deactivate under TOS to a lower extent than ZnO/Al_2O_3 and deactivation is mainly due to coke formation. In contrast to ZnO/Al_2O_3, the catalytic activity of $Zn_xAl_yO_4$ NPs can be regenerated largely (more than 90%) under airflow at 650 °C.

2. EXPERIMENTAL SECTION

2.1. Materials

γ-Al_2O_3 (≥99.9%, Alfa Aesar, $S_{BET} = 100$ m^2 g^{-1}), SiO_2 (Aerosil 300, ≥ 99.8%, Evonik, $S_{BET} = 300 \pm 30$ m^2 g^{-1}), electronic grade diethyl zinc (DEZ, ALD precursor, Pegasus Chemicals), $Zn(NO_3)_2 \cdot 6H_2O$ (98%, Acros Organics), $AlCl_3 \cdot 6H_2O$ (≥99%, Acros Organics), citric acid (≥99.8%, Acros Organics) polyethylene glycol (PEG 6000, Sigma-Aldrich), $Al(NO_3)_3 \cdot 9H_2O$ (≥95%, Acros Organics), aqueous ammonia (Fisher Scientific, 35 vol.%), acrylamide (≥99%, Acros Organics), N,N′-methylenebisacrylamide (≥99%, Sigma-Aldrich), D-(+)-glucose (extra pure, SLR, Fisher Scientific), and SiC (Alfa Aesar, 46 grit particles) were purchased from the respective commercial suppliers and used without further purification.

2.2. Synthesis

2.2.1. ALD-deposited ZnO/Al_2O_3 and ZnO/SiO_2

SiO_2 and γ-Al_2O_3 supports were mixed with water to form homogenous slurries that were dried at 120 °C overnight. The resulting chunks of SiO_2 and γ-Al_2O_3 were crushed and sieved to obtain a 150-300 μm size fraction that was used subsequently for the ALD synthesis. Deposition of ZnO on SiO_2 or γ-Al_2O_3 was carried out in a commercial ALD system (Picosun R-200) integrated in a N_2 glovebox and equipped with a POCA system, which is a reaction chamber setup used for powder coating. The powder holder with a pore size of 40 – 100 µm was filled with approximately 100 mg of support (γ-Al_2O_3 or SiO_2). For the deposition of ZnO, diethyl zinc (DEZ) and DI water were utilized. High-purity N_2 was used as both carrier and purge gas. The pulse and purge times were 0.1 s, 15 s, 0.1 s and 15 s for, subsequently, DEZ, N_2, H_2O and N_2, using three pulses for both DEZ and H_2O for a total of 10-50 cycles. The deposition temperature was 150 °C. Under these conditions, STEM analysis of ZnO coated NPs revealed a deposition rate of ca. 0.17 nm of ZnO per one ALD cycle. The as deposited materials were calcined at 700 °C (4 °C min^{-1}) for 4 h in a muffle furnace under static air. The zinc content in the calcined materials was determined using inductively coupled plasma atomic emission spectroscopy (ICP-AES) experiments and is presented in Table 1.

Table 1. BET surface area (SA) and Zn loadings of ALD-synthesized materials.

Entry	Support	ALD cycles	SA (m^2 g^{-1})	Zn (wt. %)*	Material
1	γ-Al_2O_3	10	101	1.2	10ZnO/Al_2O_3
2	γ-Al_2O_3	30	89	2.4	30ZnO/Al_2O_3
3	γ-Al_2O_3	50	93	3.3	50ZnO/Al_2O_3
4	SiO_2	10	274	2.2	10ZnO/SiO_2
5	SiO_2	30	239	7.7	30ZnO/SiO_2

*according to ICP-AES results

2.2.2. Zinc aluminate nanoparticles (NPs)

$Zn_xAl_yO_4$ nanoparticles ($Zn_xAl_yO_4$-NPs) were synthesized using a reported hydrothermal method.[24] For $Zn_{0.15}Al_{2.56}O_4$ (Zn/Al ratio according to ICP), polyethylene glycol (PEG,7.848 g, 1.31 mmol) was dissolved in DI water (100 ml) followed by the addition of $Zn(NO_3)_2 \cdot 6H_2O$ (3.245 g, 10.91 mmol) and $Al(NO_3)_3 \cdot 9H_2O$ (8.184 g, 21.82 mmol). The reaction mixture was stirred to obtain a clear solution. The molar ratio of all cations to PEG was kept constant at 25. Then, the pH was adjusted to 10.5 by the dropwise addition of an aqueous ammonia solution (35 vol. %) under continuous stirring. When the pH=10.5 was achieved, ammonia addition was stopped and the resulting solution was stirred for additional two hours. The slurry obtained was transferred to a polytetrafluoroethylene (PTFE)-lined stainless steel autoclave and aged under static air at 110 °C for three days. After cooling down to ambient conditions, the precipitate was recovered by centrifugation, washed with DI water (3 × 300 ml) and calcined at 700 °C (4 °C min^{-1}) for 4 h under static air in a muffle furnace. A similar approach was used to synthesize zinc aluminate NPs with varying Zn/Al molar ratios (see Table 2 for the ICP-AES results). A crystalline reference zinc aluminate spinel (denoted bulk-$ZnAl_2O_4$) was synthesized for the sake of comparison to aid the XAS and NMR analyses (see supporting information for synthesis details and XRD characterization).

Table 2. Zn loadings and Zn/Al ratios in $Zn_xAl_yO_4$ materials synthesized via a hydrothermal method. BET surface area of $Zn_xAl_yO_4$ materials is ca. 205 $m^2\ g^{-1}$, independent of the composition.

Entry	Material	Zn (wt.%)*	Zn/Al ratio*
1	$Zn_{0.06}Al_{2.63}O_4$	2.80	0.02
2	$Zn_{0.15}Al_{2.56}O_4$	7.04	0.06
3	$Zn_{0.42}Al_{2.39}O_4$	17.60	0.18

*according to ICP-AES

2.3. Characterization

For laboratory based X-ray powder diffraction (XRD), a PANalytical Empyrean diffractometer equipped with Bragg–Brentano HD incident beam optics and an X′Celerator Scientific ultra-fast line detector was used. K_α radiation of a Cu anode at 45 kV and 40 mA was used to perform scans in the 2θ range of 5-100° with a step size of 0.017° and acquisition time of 0.65 s per step.

Synchrotron XRD and X-ray absorption spectroscopy (XAS) were carried out at Swiss Norwegian Beam Line (SNBL, BM31) of the European Synchrotron Radiation Facility (ESRF), Grenoble, France. A Si (111) double crystal was used as a monochromator and the data were collected in transmission mode with a step size of 0.5 eV and 140 ms acquisition time within the 9.45-10.2 keV range. A DEXELA detector was used to collect the XRD data having a Si (111) channel-cut monochromator set at a wavelength (λ) of 0.493 Å.[25] Synchrotron XRD data were collected in 1 mm quartz capillaries.

In situ combined XRD-XAS studies were carried out in a quartz capillary cell (0.1 mm wall thickness outer diameter of 1.5 mm). The specimen were placed between two plugs of quartz wool in a quartz capillary that was heated by an air blower, reaching up to 750 °C (at the specimen). Prior to the measurements, the blower temperature was calibrated using an empty capillary and a thermocouple placed in the middle of the blower under a constant flow of N_2. A schematic of the beamline setup has been described elsewhere.[26, 27]

^{27}Al magic angle spinning nuclear magnetic resonance (MAS NMR) was acquired using an Avance III HD NMR spectrometer (Bruker) working at the Larmor frequency of 400 MHz for the ^1H nucleus. A 3.2 mm double resonance probe was tuned to 104.26 MHz for the ^{27}Al nuclei using spinning rates between 15-18 kHz. Materials were packed into 3.2 mm zirconia rotors in air and were spun using N_2 as bearing, drive, and VT flows. The ^{13}C signal of adamantane was used as an external secondary reference to calibrate the ppm scale of the spectra.

Scanning transmission electron microscopy and energy dispersive X-ray mapping (STEM-EDX) were acquired using a FEI Talos F200X. The operation voltage of the instrument was set to 200 kV in scanning electron microscopic (STEM) mode.

Thermogravimetric analysis (TGA) was performed in a Mettler Toledo TGA/DSC3+ instrument. The specimen was loaded into a 70 µl platinum crucible and heated to 1000 °C under synthetic air (30 ml min^{-1}) using a 10 °C min^{-1} ramp rate and kept at this temperature for 10 min.

Brunauer-Emmett-Teller (BET)[28] surface areas and Barrett-Joyner-Halenda (BJH)[29] pore size distributions were calculated using N_2 physisorption data acquired on a NOVA 4000e (Quantachrome) instrument at −196 °C. Prior to the measurement, materials were outgassed at 300 °C under vacuum for 3 h. A Thermo Fisher DXR2 Raman spectroscope equipped with a 455 nm laser reaching up to 6 mW laser power was used to collect Raman spectra. A full range grating with a resolution of 1200 lines mm^{-1} was used to collect the spectra within 100-3600 cm^{-1}. Each Raman spectrum reported here is an average of ten different points on the specimen to ensure homogeneity and reproducibility.

2.4. Catalytic tests

Prepared catalysts (100 mg, sieved fraction of 150-300 µm) were mixed with 200 mg of SiC and placed between two plugs of quartz wool on a quartz frit in a 10 mm internal diameter (12.5 outer diameter) quartz reactor. The catalytic reactivity was measured using 10 mol% C_3H_8 in N_2 in a commercial Microreactivity-Efficient catalyst test setup (PID Eng&Tech). The off-gas was analyzed by a gas chromatograph (GC, Global Analyzer Solutions) equipped with two thermal conductivity detectors (TCD) and one flame ionization detector (FID). The catalysts were heated to 600 °C (10 °C min^{-1}) under N_2 (21 ml min^{-1}), then the feed gas was introduced and GC data was collected every three minutes. Catalyst regeneration was performed after ca. 90 min of the PDH reaction by flowing synthetic air (21 ml min^{-1}) for 20 min at 650 °C, followed by a 10 min purge with N_2 (21 ml min^{-1}) while cooling down.

Propane conversion (*X*), the selectivity to gas phase products (*S*) and space-time yield were calculated according to the following equations.

$$\text{Selectivity } (S_A) = \frac{n_A F_{A\ out}}{\sum n_i F_i}$$

$$\text{Conversion } (X) = \frac{\sum F_i}{F_{C3H8\ in}}$$

$$\text{Space time yield} = \frac{F_{C3H8\ out}\left(\text{ml h}^{-1}\right) \times y_{C3H6}}{24450\left(\text{ml mmol}^{-1}\right) \times \text{catalyst weight (g)}}$$

where F_i and F_A are the flow of carbon product i and A out of the reactor in ml h^{-1}. n_i and n_A are the number of carbons in molecular formula of product i and product A. $F_{C3H8\ in}$ and $F_{C3H8\ out}$ are the propane inlet and outlet flows, respectively and F is the total flow in ml h^{-1}. Other parameters used are the molar volume of a gas at room temperature and atmospheric pressure (24450 ml $mmol^{-1}$) and y_{C3H6} is the mole fraction of propene in the products. The specific activity is defined in the ESI file.

3. RESULTS AND DISCUSSIONS

3.1. Catalysts' structure

Aiming at establishing a structure-performance relationship for zinc based, alumina-supported PDH catalysts, we set about to identify the role of the alumina support in defining the structure of Zn sites. To this end, we prepared three types of model catalysts: i) ZnO coated on γ-Al_2O_3 nanoparticles via ALD, using 10, 30, or 50 ALD cycles (denoted as 10ZnO/Al_2O_3, 30ZnO/Al_2O_3, and 50ZnO/Al_2O_3, respectively); ii) ZnO coated onto SiO_2 nanoparticles via ALD (10ZnO/SiO_2 and 30ZnO/SiO_2); iii) $Zn_xAl_yO_4$ nanoparticles (NPs) obtained via a hydrothermal method, with varying molar ratios of Zn:Al. The prepared materials were calcined at 700 °C under static air for 4h. The Zn content of each material determined by ICP, and the BET surface areas (SA) are given in Tables 1 and 2. To characterize the average and local structure of the materials, we have applied synchrotron based XRD, Zn K-edge XAS as well as STEM EDX and ^{27}Al magic angle spinning (MAS) NMR.

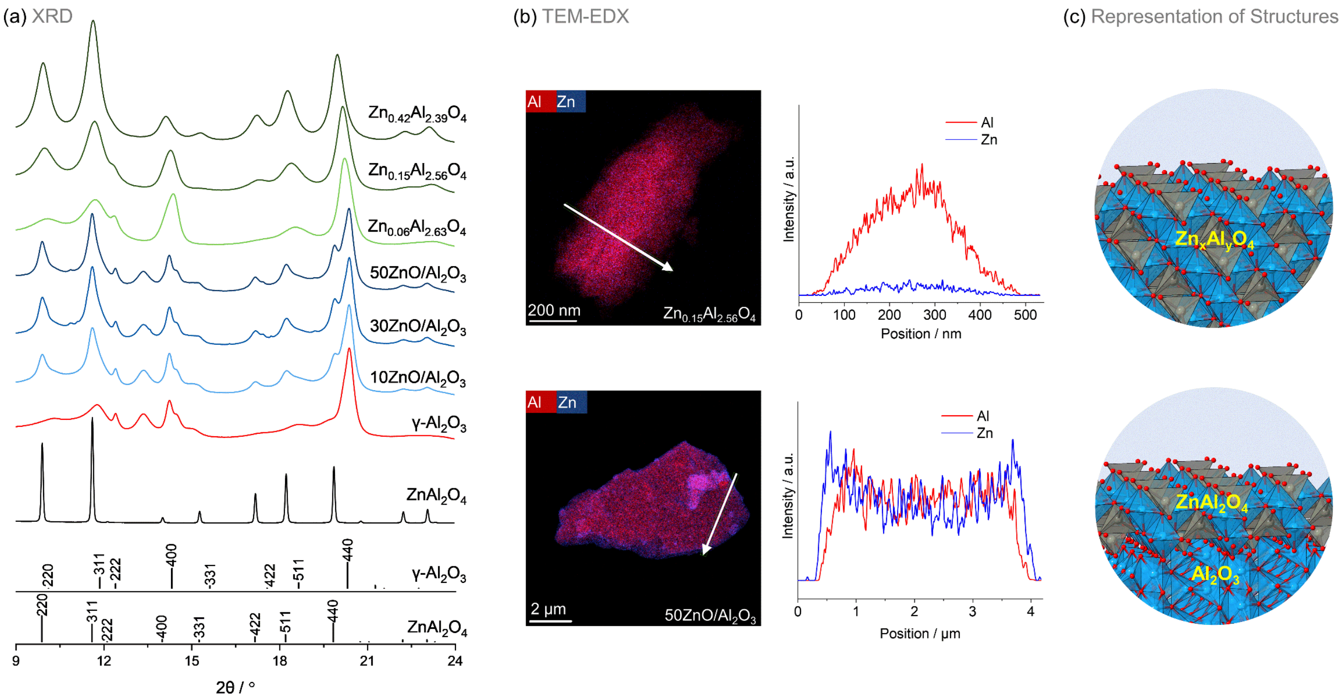

Figure 1. (a) XRD (λ=0.493 Å) and (b) STEM-EDX mapping and a line scan (the arrows indicate the EDX line scan direction) of 50ZnO/Al_2O_3 and $Zn_{0.15}Al_{2.56}O_4$ NPs. Reference bulk-$ZnAl_2O_4$ XRD data and simulated XRD patterns according to ICSD database (collection code: 26849) are plotted to aid phase identification. (c) Representation of structures of calcined $Zn_xAl_yO_4$ NPs (top) and ZnO/Al_2O_3 (bottom) PDH catalysts. Oxygen, aluminum, and zinc atoms are represented in red, blue and grey, respectively.

3.1.1. Average structure and morphology

ALD deposition of ZnO on γ-Al_2O_3 using DEZ and steam pulses at 150 °C results in the formation of a wurtzite ZnO shell on top of a γ-Al_2O_3 core (Figures S1). After calcination at 700 °C, synchrotron XRD analysis reveals the formation of a $ZnAl_2O_4$ spinel phase in ZnO/Al_2O_3 materials (Figure 1a), i.e., ZnO reacts with the γ-Al_2O_3 support forming a spinel $ZnAl_2O_4$ phase, likely via ZnO diffusion through γ-Al_2O_3.[30] $ZnAl_2O_4$ has a spinel type structure with Zn^{2+} and Al^{3+} in tetrahedral and octahedral sites, respectively. The structure of γ-Al_2O_3 is highly debated and it has been described as a defective spinel with Al^{3+} in tetrahedral and octahedral sites, yet other non-spinel models have also been proposed.[31] Albeit certain apparent resemblance between γ-Al_2O_3 and $ZnAl_2O_4$ structures exists, the diffraction patterns of each phase can be distinguished well by their peak positions and relative intensity as shown in Figure 1a.[32] For instance, the 440 diffraction peak of $ZnAl_2O_4$ is observed at lower 2θ angles (19.86°) with respect to the same reflection of γ-Al_2O_3 (20.39°), due to the difference in the cell parameters (7.911 and 8.086 Å, for $ZnAl_2O_4$ and γ-Al_2O_3, respectively).[33, 34] The XRD patterns of ZnO/Al_2O_3 materials contain discernable reflections of γ-Al_2O_3 and $ZnAl_2O_4$. The higher intensities of the 220 and 311 reflections (as compared to γ-Al_2O_3) further indicate the formation of a $ZnAl_2O_4$ phase. The relative content of $ZnAl_2O_4$ phase increases with number of ALD cycles as follows from the increasing intensity of the 440 peak of $ZnAl_2O_4$ relative to the intensity of the 440 peak of γ-Al_2O_3 (indexed for convenience according to the space group *Fd*3*m*[31] in Figure S1). We also notice a subtle peak shift (of ca. −0.03°) of the γ-Al_2O_3 peak, which can be due to the diffusion of Zn into the γ-Al_2O_3 core.

STEM-EDX and line mapping of the ZnO/Al_2O_3 materials (Figures 1b and S2) show the distribution of Zn and Al in and on the agglomerated nanoparticles. The images reveal a Zn-rich shell around an Al-rich core (see the line map in Figure 2b). Complemented with XRD results, this suggests a microstructure in which a $ZnAl_2O_4$ shell covers the γ-Al_2O_3 core (i.e., a $ZnAl_2O_4$/Al_2O_3 core-shell type structure shown schematically in Figure 1c).

Unlike core-shell ZnO/Al_2O_3 materials, $Zn_xAl_yO_4$ NPs exhibit a single-phase nanocrystalline spinel type structure. By increasing the Zn/Al ratio (Figure 1a and Table 2), the 400 diffraction peak shifts toward lower 2θ angles, indicating an increase in the cell parameter that was determined (using full profile analysis) as 7.943(2), 7.981(2) and 8.064(1) Å for $Zn_{0.06}Al_{2.63}O_4$, $Zn_{0.15}Al_{2.56}O_4$, and $Zn_{0.42}Al_{2.39}O_4$ NPs, respectively (Figure S3). STEM-EDX mapping reveals a homogeneous distribution of Zn and Al (Figure 1b and Figure S4) within the $Zn_xAl_yO_4$ NPs, in contrast to the core-shell type structure of ZnO/Al_2O_3 materials. Thus, the combined information of XRD and EDX analyses show that the $Zn_xAl_yO_4$ NP materials can be described as homogeneous $Zn_xAl_yO_4$ solid solutions.

Turning to the ZnO/SiO_2 materials, the XRD patterns show diffraction peaks due to crystalline wurtzite ZnO (*P*63*mc* space group, Figure S5). Similar to ZnO/Al_2O_3 materials, a core-shell structure can be seen also for the ALD-made ZnO/SiO_2 according to the STEM-EDX mapping results (Figure S6).

3.1.2. Local structure of Zn and Al sites

To determine coordination of Al in our materials, we use ^{27}Al MAS NMR.[35] Al sites that are tetra-, penta- and hexacoordinated with O (Al_{IV}, Al_V and Al_{VI}) give rise to distinct NMR peaks with maxima at ca. 65, 28, and 7 ppm, respectively, whereas the up-field tailing of peaks is due to the distribution of quadrupolar couplings typical for disordered structures (Figure 2a).[36, 37] Note that the ^{27}Al NMR spectrum of the reference bulk-$ZnAl_2O_4$ features a peak at ca. 10 ppm due to the Al_{VI} sites and no other notable downfield peak (Figure 2a), i.e. no Al_{IV} sites are present. Despite ongoing debate on γ-Al_2O_3 structure,[38] it contains, by experimental and computational studies, Al_{VI} and Al_{IV} sites, the former represents ca. 70 ± 2 % of all Al sites.[39] We observe peaks owing to Al_{IV} and Al_{VI} sites in γ-Al_2O_3 at ca. 64 and 8 ppm, respectively, with no discernable contribution from Al_V sites; the Al_{IV}/ Al_{IV+VI} peak ratio is ca. 0.285 (Figure S7). ^{27}Al NMR spectra of ZnO/Al_2O_3 materials also contain peaks due to Al_{IV} and Al_{VI} sites but with relative intensities that are different from γ-Al_2O_3 (Figure 2a). With an increasing number of ALD cycles, the intensity of the Al_{IV} peak at ca. 64 ppm decreases, in line with the substitution of Al_{IV} sites by Zn_{IV} sites in the spinel lattice, forming $ZnAl_2O_4$. This is reflected in a change in the Al_{IV} / Al_{IV+VI} peak area ratio that decreases from 0.283 to 0.280 and to 0.275 in 10, 30, and 50ZnO/Al_2O_3, respectively (Figure S7). If we assume that all zinc only occupies Al_{IV} sites and Al takes both Al_{IV} and Al_{VI} sites in γ-Al_2O_3, the expected values for the Al_{IV} / Al_{IV+VI} peak ratio are 0.278, 0.271, and 0.265 for 10, 30, and 50ZnO/Al_2O_3, respectively. The slight discrepancy between the experimentally and theoretically-determined ratios might be explained by the error arising from the NMR peak fitting (Figure S7).

For $Zn_xAl_yO_4$ NPs, we also observed two peaks due to Al_{IV} and Al_{VI} sites. The intensity of the ^{27}Al NMR peak due to Al_{IV} sites (ca. 64 ppm) decreases with increasing Zn/Al ratio (Figure 2a). The ratio Al_{IV} / Al_{IV+VI} was determined to decrease with increasing Zn content, as 0.32, 0.27, and 0.17 for $Zn_{0.06}Al_{2.63}O_4$, $Zn_{0.15}Al_{2.56}O_4$, and $Zn_{0.42}Al_{2.39}O_4$ NPs, respectively (Figure S8).

The local structure of the Zn sites was investigated using Zn K-edge XANES and EXAFS analyses. The Zn K-edge XANES spectra of the ZnO/Al_2O_3 materials are shown in Figure 2b. Five distinct features centered at ca. 9665, 9670, 9674, 9681, and 9688 eV, labeled as A-E, can be distinguished (Figure 2b). These features agree well with the XANES spectrum of the reference bulk-$ZnAl_2O_4$ (see also Figure S9), whereas the reference wurtzite ZnO exhibits a broad XANES feature centered at 9670 eV (Figure 2b, inset). While zinc is in a tetrahedral coordination in both wurtzite ZnO and spinel bulk-$ZnAl_2O_4$, the clear differences in the corresponding XANES features evidence the different local environments of zinc in these two structures (spinel aluminate and wurtzite, inset in Figure 2b).[40]

The Fourier transformed (FT) EXAFS data of ZnO/Al_2O_3 materials show a first coordination shell that is attributed to Zn−O, and a second coordination shell which contains Zn−Al/Zn−Zn sub-shells (Figure 2c). Note that the amplitude of the second peak decreases with the number of ZnO ALD cycles, being in all cases lower than that in the bulk-$ZnAl_2O_4$. A quantitative description of the local environment is obtained by EXAFS fittings (Table S1). The fittings show a Zn−O coordination sphere at ca. 1.95 Å, with a coordination number (CN) that is similar (within standard deviation of the method) and close to 4 (3.5-3.9) in the three ZnO/Al_2O_3 materials. The second coordination sphere consists mainly of Zn-Al and Zn-Zn shells at distances of ca. 3.38-3.37 Å. By increasing the number of ALD cycles from 10 to 30 and 50, the CN for the Zn-Zn sphere increases from 3(1) to 4(1) while the CN for Zn-Al decreases significantly, i.e. from 7(2) to 5(1) and further to 4(1) (Table S1). A plausible explanation for this observed increase in CN as Zn content decreases, notably in 10ZnO/Al_2O_3, is that a larger portion of Zn atoms is found in the bulk or subsurface layers in 10ZnO/Al_2O_3 relative to 30 and 50ZnO/Al_2O_3 due to a deeper diffusion of Zn (Zn atoms at the surface are less coordinated than in the bulk).

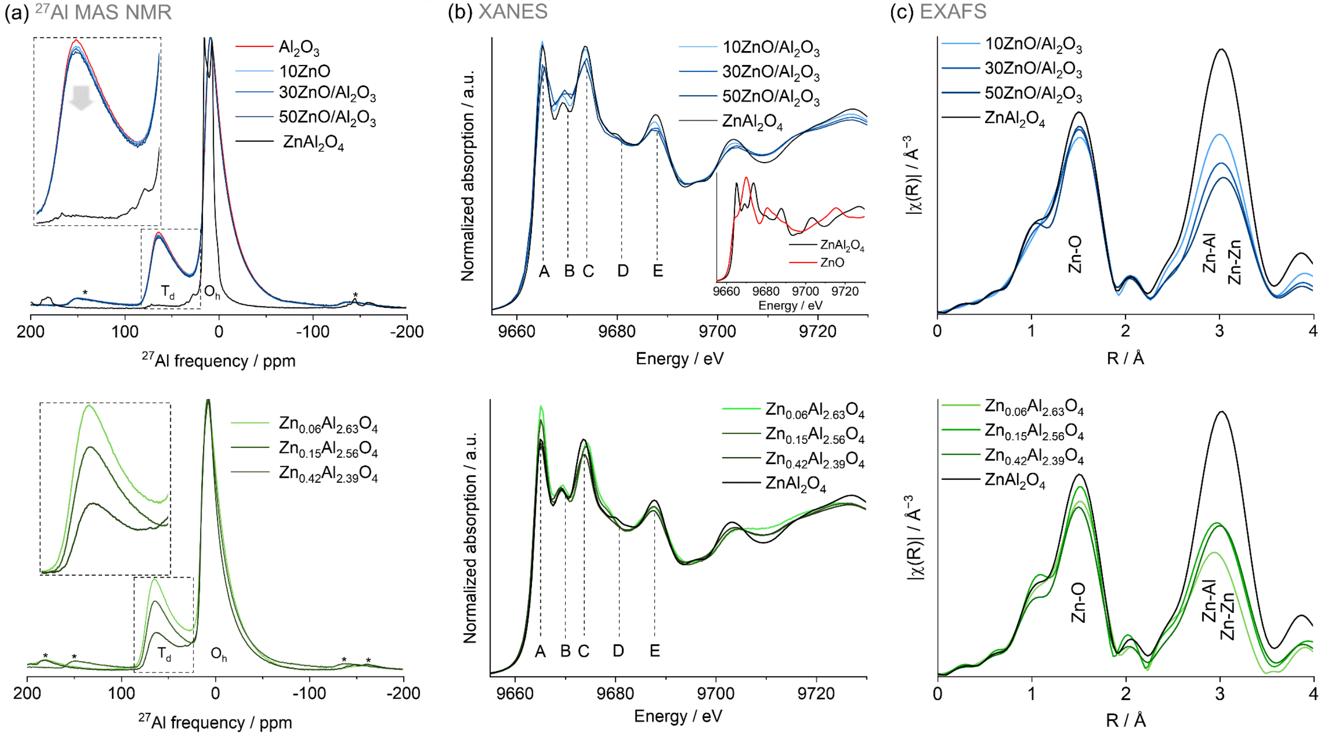

Figure 2. (a) ^{27}Al MAS NMR; (b) Zn K-edge XANES; (c) EXAFS of calcined (700°C) ZnO/Al_2O_3 and $Zn_xAl_yO_4$ NPs. Inset in (b) shows the XANES patterns of the two references bulk-$ZnAl_2O_4$ and wurtzite ZnO. All measurement are conducted under atmospheric conditions. For ^{27}Al MAS NMR, 15-18 kHz spinning rates were used, side bands are marked by asterisks, and all spectra are normalized to the peak maximum at ca. 8 ppm (Al_{VI} sites).

The thermally driven phase transformation in $50ZnO/Al_2O_3$ during calcination was followed by an in situ XRD-XAS experiment (50-750 °C, in air-flow, Figure S10).[26, 41] Initially, the XANES spectrum of the as prepared $50ZnO/Al_2O_3$ showed distinct features due to ZnO (feature B at 9670 eV), in line with XRD data. Upon heating, the intensity of feature B decreases continuously while features A and C grow, indicating the gradual formation of $ZnAl_2O_4$ (Figure S10). Linear combination fitting analysis shows that the transformation begins at 400 °C and proceeds continuously with time and temperature (Figure S10). However, in the in situ cell we did not observe the full conversion of ZnO into $ZnAl_2O_4$ within the temperature range and time duration studied, very likely due to differences in the heat transfer between the laboratory furnace and the in situ cell in combination with a limited calcination time. In situ XRD data shows the appearance of Bragg peaks due to $ZnAl_2O_4$ for $T > 700$ °C, which grow in intensity while the magnitude of the ZnO peaks decreases, in line with XANES analysis. Overall, the combined in situ XRD-XAS experiments confirm the transformation of the ZnO shell (on γ-Al_2O_3) into a $ZnAl_2O_4$ shell (on a γ-Al_2O_3 core).

The XANES spectra of $Zn_xAl_yO_4$ NPs show similar features as the reference bulk-$ZnAl_2O_4$, with the A and C features in the XANES spectra of $Zn_xAl_yO_4$ NPs increase with a decreasing Zn/Al ratio (Figure 2b), possibly due to subtle difference in the local environment of Zn (i.e., richer in Al as with decreasing the Zn/Al ratio). The FT-EXAFS data are shown in Figure 2c and the fitting results are presented in Table S1. The Zn−O, Zn−Al, and Zn−Zn spheres are located at ca. 1.95, 3.34, and 3.52 Å, respectively (i.e. similar distances as the ones observed for the ZnO/Al_2O_3 materials). The CN for Zn−O is largely unaffected by changes in the ratio Zn:Al in the $Zn_xAl_yO_4$ NPs and vary in the range 3.5-3.9, consistent with Zn occupying Zn_{IV} sites independent of the Zn/Al ratio (Table S1). Only a slight variation in the CN number for the second coordination sphere was observed with varying Zn content. The CNs for Zn−Al are between 5(1) and 6(1), whereas the CN for Zn−Zn increases from 2(1) to 3(1) and remains constant at 3(1) for $Zn_{0.06}Al_{2.63}O_4$, $Zn_{0.15}Al_{2.56}O_4$, and $Zn_{0.42}Al_{2.39}O_4$ NPs, respectively.

The XANES spectrum of $30ZnO/SiO_2$ is very similar to that of the reference wurtzite ZnO, with Zn sites in T_d coordination (Figure S5), in line with XRD data. Furthermore, the presence of the second coordination shell (Zn−Zn) in the EXAFS data of $30ZnO/SiO_2$ (Figure S5) is consistent with the formation of a supported ZnO phase (Figure S5). The intensity of the first coordination shell (Zn−O) in $30ZnO/SiO_2$ is similar to that of the ZnO reference (Figure S5).

3.2. PDH catalytic performance

3.2.1. Initial catalytic activity

All catalysts as well as the bare supports were tested for PDH in a plug-flow reactor at 600 °C using 10 mol.% C_3H_8 in N_2 (WHSV = 22.7 g C_3H_8 g_{cat}^{-1} h^{-1}). Figure 3a plots the initial activities expressed as space time yields (STY, mmol C_3H_6 g_{cat}^{-1} h^{-1}) and product selectivities for the studied materials (see also Table S2 detail catalytic results showing product distribution in molar fraction). While C_3H_6 is the main product of the PDH reaction, C_2H_6, CH_4 and C_2H_4 were also observed as byproducts.[4] The highest initial STY and selectivity were observed for $50ZnO/Al_2O_3$ and $Zn_{0.15}Al_{2.56}O_4$-NPs (Figure 3a).

$30ZnO/SiO_2$ showed a poor catalytic activity (4.4 mmol C_3H_6 g_{cat}^{-1} h^{-1}) and a low C_3H_6 selectivity (58%), i.e., values that are comparable to those of the bare SiO_2 support (Figures 3 and S11). These results are in line with previous studies showing that wurtzite ZnO containing Zn_{IV}-O-Zn_{IV} linkages exhibits a poor activity for PDH.[21, 42]

The activity and selectivity of the ZnO/Al_2O_3 catalysts increased with increasing Zn content, i.e., with increasing content of the $ZnAl_2O_4$ phase (Figure 3a and Figure S12). The initial STY and propene selectivity decreased as follows: $50ZnOAl_2O_3$ > $30ZnO/Al_2O_3$ > $10ZnO/Al_2O_3$ (entries 1-3, Table 3). These results show that the spinel $ZnAl_2O_4$ phase formed on top of a γ-Al_2O_3 core, as revealed by XRD and XAS analysis, catalyzes the PDH reaction. Spinel $ZnAl_2O_4$ contains Zn_{IV}-O-$Al_{VI/IV}$ linkages, which are presumably the active sites for PDH reaction in zinc aluminate catalysts. Thus, a dissolution of poorly active ZnO into γ-Al_2O_3 forms $ZnAl_2O_4$ with tetrahedral Zn^{2+} sites in close proximity to Al sites, leading to an increased activity and selectivity in PDH relative to the $30ZnO/SiO_2$ reference.

Table 3. Catalytic data for the studied materials with TOS indicated in the subscript.

Entry	Catalyst	$X_{3\ min}$ [a] (%)	$S_{C3H6\text{-}3\ min}$ [b] (%)	$STY_{3\ min}$ [c]	Specific activity$_{3\ min}$ [d]	$S_{C3H6\text{-}90\ min}$ [e] (%)	$STY_{90\ min}$ [e]	$S_{C3H6\text{-}270\ min}$ [f] (%)	$STY_{270\ min}$ [f]
1	$10ZnO/Al_2O_3$	5.0	59	4.1	0.6	59	4.1	59	4.1
2	$30ZnO/Al_2O_3$	9.6	68	5.9	5.2	60	4.4	60	4.4
3	$50ZnO/Al_2O_3$	17.2	77	9.0	9.8	61	4.3	60	4.2
4	$Zn_{0.06}Al_{2.63}O_4$	9.5	68	4.3	2.8	65	4.2	65	–
5	$Zn_{0.15}Al_{2.56}O_4$	16.7	75	8.0	3.7	66	5.3	65	5.2
6	$Zn_{0.42}Al_{2.39}O_4$	18.4	65	7.1	1.5	62	5.0	62	–
7	$30ZnO/SiO_2$	5.5	59	4.4	0.3	59	4.4	–	–

[a] X stands for C_3H_8 conversion

[b] S_{C3H6} stands for propene selectivity among gaseous products

[c] in units mmol C_3H_6 g_{cat}^{-1} h^{-1}

[d] in units mol C_3H_6 (mol Zn h)$^{-1}$. Specific activity is after the subtraction of the uncatalyzed background reaction. See the ESI file.

[e] Continuous without regeneration

[f] Continuous with two regeneration cycles every 90 min

The specific activity, defined as mol C_3H_6 (mol Zn h)$^{-1}$ (see supporting information for details), calculated based on the ICP-determined amount of zinc, also shows an increasing specific activity rate with an increasing number of ALD cycles: 50ZnO/Al_2O_3 > 30ZnO/Al_2O_3 > 10ZnO/Al_2O_3 (entries 1-3 Table 3). The low specific activity of 10ZnO/Al_2O_3 can be explained by the deeper diffusion of Zn into the inner layers of alumina, as suggested by EXAFS analysis, which decreases the density of active surface sites for the PDH reaction.

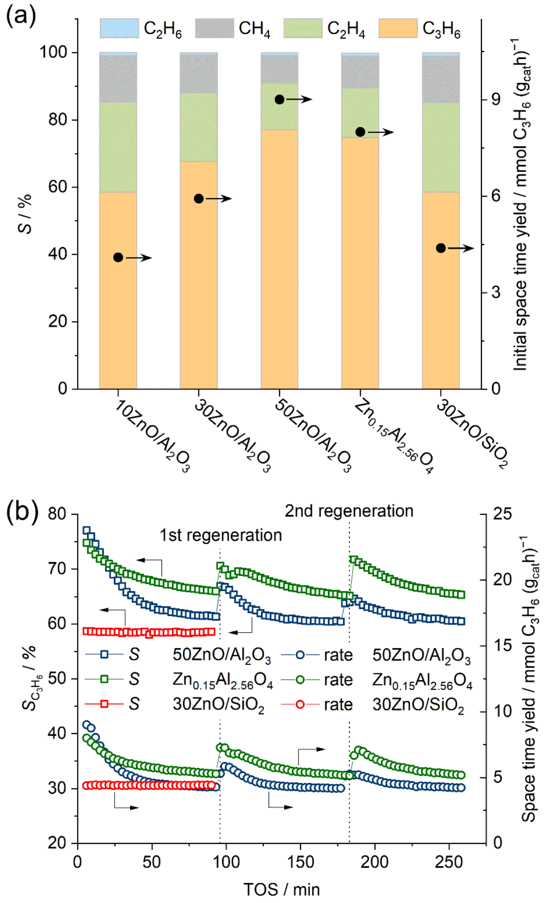

Figure 3. (a) Initial space-time yields of the studied materials. (b) Propene selectivity and STY data during 270 min TOS including two regeneration cycles after 90 min for selected catalysts. A total flow of 21 ml min^{-1}, 10 mol.% C_3H_8 in N_2, at 600 °C and synthetic air at 650 °C was used for reaction and regeneration, respectively.

In the case of $Zn_xAl_yO_4$-NPs, the highest space-time yield and propene selectivity were observed for $Zn_{0.15}Al_{2.56}O_4$-NPs (Table 3 entry 4 and Figure S13), while all of the three studied NP compositions showed higher selectivities and activities than 30ZnO/SiO_2 and the bare supports. $Zn_{0.42}Al_{2.39}O_4$-NPs show a higher conversion when compared to $Zn_{0.15}Al_{2.56}O_4$-NPs, yet the latter was more selective towards propene (Figure S13). Thus, zinc aluminate solid solutions containing Zn_{IV}-O-$Al_{VI/IV}$ sites are catalytically active for PDH, while $Zn_{0.15}Al_{2.56}O_4$ (among the materials tested in this work) contains an optimal ratio of Zn_{IV}, Al_{IV} and Al_{VI} sites. In addition, the lower specific activity (mol C_3H_6 (mol$_{Zn}$ h)$^{-1}$, Figure S14) of $Zn_{0.15}Al_{2.56}O_4$-NPs (solid solution) relative to 50ZnO/Al_2O_3 (core-shell microstructure) is explained by a higher density of Zn_{IV}-O-$Al_{VI/IV}$ linkages on the surface of 50ZnO/Al_2O_3.

3.2.2. Catalytic performance with TOS

Next, we compare the catalytic performance during TOS for the materials that showed the highest initial activity, i.e., 50ZnO/Al_2O_3 and $Zn_{0.15}Al_{2.56}O_4$ NPs (Figure 3b). A regeneration step (20 min under a flow of synthetic air at 650 °C followed by 10 min of purging with N_2) was introduced after 90 min of the PDH reaction. In the first PDH cycle, both $Zn_{0.15}Al_{2.56}O_4$-NPs and 50ZnO/Al_2O_3 deactivate with TOS. Notably, the deactivation rate (defined as deactivation rate = 1 – STY at 90 min / STY at 3 min × 100)[18] of the $Zn_{0.15}Al_{2.56}O_4$ NPs is lower than that of ALD 50ZnO/Al_2O_3, determined as 34 and 52 %, respectively (Table S3 and Figure 3b). In ZnO/SiO_2, no changes were observed by TOS with respect to its catalytic activity that was similar to that of bare SiO_2.

Each regeneration cycle restores largely the initial STY of $Zn_{0.15}Al_{2.56}O_4$ NPs, (92% and 90% in the 2nd and 3rd cycles, respectively). In contrast, for 50ZnO/Al_2O_3 a decrease in the initial catalytic activity after each regeneration cycle was observed (65% and 57% of the initial catalytic activity in the 2nd and 3rd cycles, respectively, Figure 3b and S12); leading to an almost complete deactivation of the catalyst in the 3rd cycle. Thus, the limited regenerability of 50ZnO/Al_2O_3 by air indicates that coke formation is not the only mechanism responsible for the deactivation of the 50ZnO/Al_2O_3 catalyst with TOS.

3.3. Deactivation routes

The nature of the coke deposited on the used catalysts was characterized by TGA and Raman spectroscopy. Used catalysts were treated under air (30 ml min^{-1}) between room temperature and up to 1000 °C in a TGA while the weight loss was recorded (Figure S15 and Table S3). More than 96% of the weight loss due to carbon combustion takes place before 650 °C. The amount of the coke formed (after the first cycle of reaction) on the $Zn_{0.15}Al_{2.56}O_4$ NPs was higher than that on 50ZnO/Al_2O_3 according to TGA data, the respective weight losses were 5.1% vs 1.9% while amount of the coke formed per surface area of the catalyst were similar and equal to 0.25 and 0.20 mg m^{-2}, respectively (Figure S16, Table S3). Thus, the amount of coke formed does not correlate with the observed deactivation rates.[2, 11] Raman spectra of the spent catalysts after the 1st and 3rd cycle (Figure S17-S18 and Table S3) show two distinct Raman bands at ca. 1341 and 1600 cm^{-1}, assigned to the D and G bands of carbon;[43] the lower intensity peaks at higher wavenumbers (ca. 2920 and 3200 cm^{-1}) might be due to the D bands of graphite.[44, 45] The ratio between intensities of the D and G bands (I_D/I_G) can be used to estimate the degree of crystallinity of the carbon deposited, as the D band arises from disordered carbon (e.g. amorphous carbon) while the G band is due to the stretching mode of the sp^2 bonds in ordered graphite.[46-48] After the first PDH reaction cycle (TOS = 90 min) the I_D/I_G ratio of the $Zn_{0.15}Al_{2.56}O_4$ NPs was higher compared to 50ZnO/Al_2O_3, i.e., 1.6 vs 0.9, respectively indicative of the formation of a more amorphous carbon on the $Zn_{0.15}Al_{2.56}O_4$ NPs. A similar trend was observed after 270 min of PDH reaction (3rd cycle), the I_D/I_G ratio was 2.8 vs 2.1 for $Zn_{0.15}Al_{2.56}O_4$ NPs and 50ZnO/Al_2O_3, respectively (Figure S17-S18 and Table S3).

Since the 50ZnO/Al_2O_3 catalyst could not be fully regenerated via air treatment, a second (irreversible) deactivation mechanism is at play. We considered three hypotheses: i) reduction and/or ii) volatilization of Zn^{2+} sites and iii) diffusion of the zinc sites to the inner layers of the alumina support. All mechanisms can decrease the amount of available active Zn sites for the PDH reaction and result in deactivation (it is worth mentioning that the observed activity and selectivity is a combination of non-selective thermal cracking and selective PDH, therefore, any blocking of active PDH sites will decrease both activity and selectivity). To assess the validity of the first hypothesis, we probed changes in the oxidation state of Zn in $50ZnO/Al_2O_3$ during PDH using in situ XAS (Figure S19). Interestingly, no appreciable changes in the XANES spectra during the PDH reaction were observed (constant edge jump). This result rules out the reduction of zinc as a deactivation mechanism in this catalyst. For the second hypothesis, ICP-AES results of the used catalysts do not show a significant change in the zinc content of the samples before and after PDH reaction (270 min TOS including two regeneration cycles every 90 min, Table S4), thus ruling out the volatilization as a deactivation mechanism.

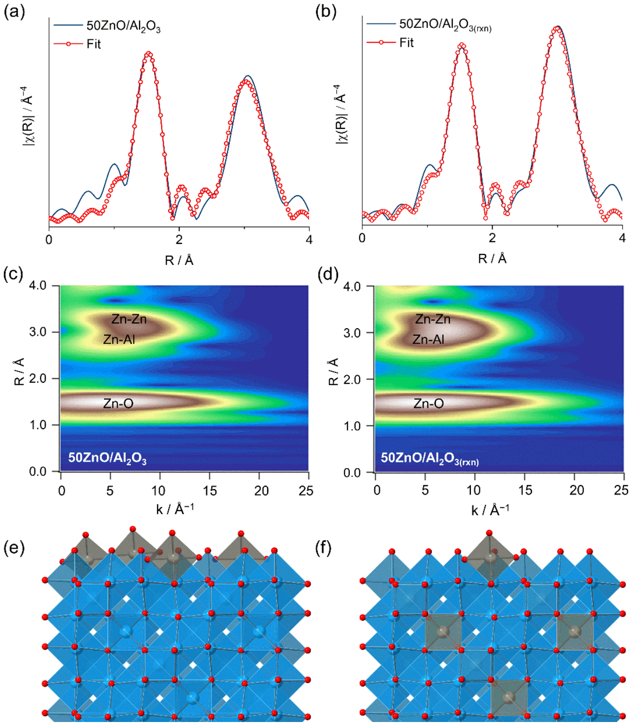

Figure 4. EXAFS-FT and fittings for $50ZnO/Al_2O_3$ (a) before and (b) after the PDH reaction with the respective wavelet analysis presented in panels (c) and (d) and schematic representation of (e) the surface and (f) the diffusion of Zn sites. The used catalyst denoted by subscript (rxn) has been studied after 270 min TOS (600 °C, 10 mol.% C_3H_8 in N_2) including two regeneration cycles (21 ml min^{-1} air at 650 °C) after 90 minutes of TOS. All data are collected under ambient conditions. Oxygen, aluminum, and zinc atoms are represented in red, blue, and grey, respectively.

Next, to probe possible structural transformation during PDH we analyzed the XRD patterns and XAS spectra (ex situ) of $50ZnO/Al_2O_3$ before and after 3 PDH reaction-regeneration cycles ($50ZnO/Al_2O_{3(rxn)}$). XRD and XANES data showed subtle changes (in Figure S20 a small shift in peaks position can be observed in the XRD data) while a more noticeable change was detected in the EXAFS data of $50ZnO/Al_2O_{3(rxn)}$ as compared with $50ZnO/Al_2O_3$, suggesting a change in the local environment of Zn upon reaction-regeneration cycles. Figure 4 shows the Fourier transform (FT) and wavelet transform (WT) of the EXAFS function of $50ZnO/Al_2O_3$ and $50ZnO/Al_2O_{3(rxn)}$. WT analysis of the EXAFS data can resolve contributions of different backscattering atoms that are at similar distances to the scattering atom.[15, 49] There is a clear increase in the peak intensity of the second coordination shell in $50ZnO/Al_2O_{3(rxn)}$ that is attributed to Zn–Al (the amplitude of the second coordination sphere in the FT of $50ZnO/Al_2O_{3(rxn)}$ becomes similar to that of poorly active $10ZnO/Al_2O_3$, Figure S21). The fitting of the EXAFS shows an increase in the coordination number (CN) of Zn–Al after reaction (from 4(1) to 6(1), Table S1) while the Zn–Zn coordination number remains almost constant, i.e. it changed from 2.1 to 2.3 (Table S1). As the atoms at the surface of the nanoparticles are less coordinated than in the bulk, such a decrease in the CN could be linked to the diffusion of zinc from the surface to the inner layers of γ-Al_2O_3 (schematic in Figure 4e-f), leading to a surface that is depleting in Zn, thus reducing the number of available active sites for the PDH reaction. The fact that changes in the XRD are less detectable, indicates that the restructuring involves Zn surface atoms diffusing to the subsurface of the particles rather than a bulk transformation. In contrast, we did not observe a notable change in the EXAFS data of $Zn_{0.15}Al_{2.56}O_4$ before and after the reaction (Figure S22), likely because Zn in this catalyst is distributed homogeneously across the bulk (and the surface) of nanoparticles already in the calcined sate, as shown by STEM-EDX.

4. CONCLUSIONS

Model catalysts were synthesized using ALD deposition of ZnO on γ-Al_2O_3 and Aerosil silica to investigate the active phase and deactivation pathways of Zn/Al_2O_3-based PDH catalysts. Calcination of ZnO/Al_2O_3 forms $ZnAl_2O_4$ layers on the γ-Al_2O_3 support, leading to a core-shell structure. While $30ZnO/SiO_2$ was inactive, the higher (still moderate) catalytic activity and selectivity observed for $50ZnO/Al_2O_3$ can be attributed to the presence of a spinel $ZnAl_2O_4$ phase. Nanoparticles of zinc aluminate (solid solutions) display similar initial catalytic activities (8 mmol C_3H_6 g_{cat}^{-1} h^{-1}) to that of ALD-made ZnO/Al_2O_3 materials (9 mmol C_3H_6 g_{cat}^{-1} h^{-1}). Our results show that zinc aluminate spinel, usually considered as an unreactive neutral support, contains Zn_{IV}-O-$Al_{VI/IV}$ linkages that enable the dehydrogenation of propane (demonstrated at 600 ºC). However, we have also identified deactivation routes of the ZnO/Al_3O_3 system. We propose, based on a combination of spectroscopic techniques, that besides coke formation, the diffusion of surface zinc into the inner layers of the alumina is an additional deactivation route for ZnO/Al_2O_3 catalysts during the PDH reaction. However, the deactivation mechanism of Zn diffusion is less probable in homogeneous solid solution catalyst. This study shows how a combination of characterization techniques that assess the average and local structure can provide detailed information on the processes that occur at the atomic level during catalysts activation (calcination) and deactivation.

ASSOCIATED CONTENT

The Supporting Information is available free of charge on the ACS Publications website and it contains experimental details, XRD, ^{27}Al MAS NMR, Raman, XAS, ICP, STEM-EDX, and TGA data.

AUTHOR INFORMATION

Corresponding Author

*E-mail: abdalap@ethz.ch (P.M.A.).

*E-mail: muelchri@ethz.ch (C.R.M.).

Author Contributions

The manuscript was written through contributions of all authors. All authors have given approval to the final version of the manuscript.

Funding Sources

We acknowledge partial funding of this work by the Swiss National Science Foundation (SNF 200021_196943).

Notes

The authors declare no competing financial interest.

ACKNOWLEDGMENT

We gratefully acknowledge the Scientific Centre for Optical and Electron Microscopy (ScopeM) of ETH Zürich for providing access to the electron microscopes. The Swiss Norwegian Beamlines (SNBL) at European Synchrotron Facilities (ESRF) is acknowledged for providing access to the synchrotron facility. Dr. Wouter van Beek is acknowledged for his assistance during beamtime. We thank Dr. Kim Sung Min for his assistance during the synthesis of ALD-made materials.

REFERENCES

1. Ceresana Propylene Market Report. https://www.ceresana.com/en/market-studies/chemicals/propylene/ (accessed March 2021).
2. Sattler, J. J. H. B.; Ruiz-Martinez, J.; Santillan-Jimenez, E.; Weckhuysen, B. M., Catalytic Dehydrogenation of Light Alkanes on Metals and Metal Oxides. *Chem. Rev.* **2014,** *114*, 10613-10653.
3. Langeslay, R. R.; Kaphan, D. M.; Marshall, C. L.; Stair, P. C.; Sattelberger, A. P.; Delferro, M., Catalytic Applications of Vanadium: A Mechanistic Perspective. *Chem. Rev.* **2019,** *119*, 2128-2191.
4. Bhasin, M. M.; McCain, J. H.; Vora, B. V.; Imai, T.; Pujadó, P. R., Dehydrogenation and oxydehydrogenation of paraffins to olefins. *Appl. Catal. A* **2001,** *221*, 397-419.
5. Wang, Y.; Su, H.; Gu, Y.; Song, X.; Zhao, J., Carcinogenicity of chromium and chemoprevention: a brief update. *OncoTargets Ther.* **2017,** *10*, 4065-4079.
6. McFarland, E., Unconventional Chemistry for Unconventional Natural Gas. *Science* **2012,** *338*, 340-342.
7. Coperet, C., C−H Bond Activation and Organometallic Intermediates on Isolated Metal Centers on Oxide Surfaces. *Chem. Rev.* **2010,** *110*, 656-680.
8. Serykh, A. I.; Agafonov, Y. A., On the nature of active sites in alumina-supported zinc propane dehydrogenation catalysts. *Mol. Catal.* **2020,** *493*, 111055.
9. Han, S.; Zhao, D.; Otroshchenko, T.; Lund, H.; Bentrup, U.; Kondratenko, V. A.; Rockstroh, N.; Bartling, S.; Doronkin, D. E.; Grunwaldt, J.-D.; Rodemerck, U.; Linke, D.; Gao, M.; Jiang, G.; Kondratenko, E. V., Elucidating the Nature of Active Sites and Fundamentals for their Creation in Zn-Containing ZrO_2–Based Catalysts for Nonoxidative Propane Dehydrogenation. *ACS Catal.* **2020,** *10*, 8933-8949.
10. Tan, S.; Gil, L. B.; Subramanian, N.; Sholl, D. S.; Nair, S.; Jones, C. W.; Moore, J. S.; Liu, Y.; Dixit, R. S.; Pendergast, J. G., Catalytic propane dehydrogenation over In_2O_3–Ga_2O_3 mixed oxides. *Appl. Catal. A-Gen.* **2015,** *498*, 167-175.
11. Hu, B.; Kim, W.-G.; Sulmonetti, T. P.; Sarazen, M. L.; Tan, S.; So, J.; Liu, Y.; Dixit, R. S.; Nair, S.; Jones, C. W., A Mesoporous Cobalt Aluminate Spinel Catalyst for Nonoxidative Propane Dehydrogenation. *ChemCatChem* **2017,** *9*, 3330-3337.
12. Zhao, D.; Lund, H.; Rodemerck, U.; Linke, D.; Jiang, G.; Kondratenko, E. V., Revealing fundamentals affecting activity and product selectivity in non-oxidative propane dehydrogenation over bare Al_2O_3. *Catal. Sci. Technol.* **2021**, *11*,1386-1394
13. Castro-Fernández, P.; Mance, D.; Liu, C.; Moroz, I. B.; Abdala, P. M.; Pidko, E. A.; Copéret, C.; Fedorov, A.; Müller, C. R., Propane Dehydrogenation on Ga_2O_3-Based Catalysts: Contrasting Performance with Coordination Environment and Acidity of Surface Sites. *ACS Catal.* **2021,** *11*, 907-924.
14. Schweitzer, N. M.; Hu, B.; Das, U.; Kim, H.; Greeley, J.; Curtiss, L. A.; Stair, P. C.; Miller, J. T.; Hock, A. S., Propylene Hydrogenation and Propane Dehydrogenation by a Single-Site Zn^{2+} on Silica Catalyst. *ACS Catal.* **2014,** *4*, 1091-1098.
15. Searles, K.; Siddiqi, G.; Safonova, O. V.; Copéret, C., Silica-supported isolated gallium sites as highly active, selective and stable propane dehydrogenation catalysts. *Chem. Sci.* **2017,** *8*, 2661-2666.
16. Dai, Y.; Gu, J.; Tian, S.; Wu, Y.; Chen, J.; Li, F.; Du, Y.; Peng, L.; Ding, W.; Yang, Y., γ-Al_2O_3 sheet-stabilized isolate Co^{2+} for catalytic propane dehydrogenation. *J. Catal.* **2020,** *381*, 482-492.
17. Chen, M.; Xu, J.; Su, F.-Z.; Liu, Y.-M.; Cao, Y.; He, H.-Y.; Fan, K.-N., Dehydrogenation of propane over spinel-type gallia–alumina solid solution catalysts. *J. Catal.* **2008,** *256*, 293-300.
18. Liu, G.; Zeng, L.; Zhao, Z.-J.; Tian, H.; Wu, T.; Gong, J., Platinum-Modified ZnO/Al_2O_3 for Propane Dehydrogenation: Minimized Platinum Usage and Improved Catalytic Stability. *ACS Catal.* **2016,** *6*, 2158-2162.
19. Zhao, D.; Li, Y.; Han, S.; Zhang, Y.; Jiang, G.; Wang, Y.; Guo, K.; Zhao, Z.; Xu, C.; Li, R., ZnO Nanoparticles Encapsulated in Nitrogen-Doped Carbon Material and Silicalite-1 Composites for Efficient Propane Dehydrogenation. *Iscience* **2019,** *13*, 269-276.
20. Gong, T.; Qin, L.; Lu, J.; Feng, H., ZnO modified ZSM-5 and Y zeolites fabricated by atomic layer deposition for propane conversion. *Phys. Chem. Chem. Phys.* **2016,** *18*, 601-614.
21. Camacho-Bunquin, J.; Aich, P.; Ferrandon, M.; "Bean" Getsoian, A.; Das, U.; Dogan, F.; Curtiss, L. A.; Miller, J. T.; Marshall, C. L.; Hock, A. S.; Stair, P. C., Single-site zinc on silica catalysts for propylene hydrogenation and propane dehydrogenation: Synthesis and reactivity evaluation using an integrated atomic layer deposition-catalysis instrument. *J. Catal.* **2017,** *345*, 170-182.
22. Almutairi, S. M. T.; Mezari, B.; Magusin, P. C. M. M.; Pidko, E. A.; Hensen, E. J. M., Structure and Reactivity of Zn-Modified ZSM-5 Zeolites: The Importance of Clustered Cationic Zn Complexes. *ACS Catal.* **2012,** *2*, 71-83.
23. Pidko, E. A.; van Santen, R. A., Activation of Light Alkanes over Zinc Species Stabilized in ZSM-5 Zeolite: A Comprehensive DFT Study. *J. Phys. Chem. C* **2007,** *111*, 2643-2655.
24. Wang, C.; Fan, W.-B.; Liu, Z.-T.; Lu, J.; Liu, Z.-W.; Qin, Z.-F.; Wang, J.-G., The dehydrogenation of ethylbenzene with CO_2 over $V_2O_5/Ce_xZr_{1-x}O_2$ prepared with different methods. *J. Mol. Catal. A: Chem* **2010,** *329*, 64-70.
25. Abdala, P. M.; Mauroy, H.; Van Beek, W., A large-area CMOS detector for high-energy synchrotron powder diffraction and total scattering experiments. *J. Appl. Crystallogr.* **2014,** *47* (1), 449-457.
26. Tsoukalou, A.; Abdala, P. M.; Stoian, D.; Huang, X.; Willinger, M.-G.; Fedorov, A.; Müller, C. R., Structural Evolution and Dynamics of an In_2O_3 Catalyst for CO_2 Hydrogenation to Methanol: An Operando XAS-XRD and In Situ TEM Study. *J. Am. Chem. Soc.* **2019,** *141*, 13497-13505.
27. Kim, S. M.; Abdala, P. M.; Margossian, T.; Hosseini, D.; Foppa, L.; Armutlulu, A.; van Beek, W.; Comas-Vives, A.; Copéret, C.; Müller, C., Cooperativity and Dynamics Increase the Performance of NiFe Dry Reforming Catalysts. *J. Am. Chem. Soc.* **2017,** *139*, 1937-1949.
28. Brunauer, S.; Emmett, P. H.; Teller, E., Adsorption of Gases in Multimolecular Layers. *J. Am. Chem. Soc.* **1938,** *60*, 309-319.
29. Barrett, E. P.; Joyner, L. G.; Halenda, P. P., The Determination of Pore Volume and Area Distributions in Porous Substances. I. Computations from Nitrogen Isotherms. *J. Am. Chem. Soc.* **1951,** *73*, 373-380.
30. Fan, H. J.; Knez, M.; Scholz, R.; Hesse, D.; Nielsch, K.; Zacharias, M.; Gösele, U., Influence of Surface Diffusion on the Formation of Hollow Nanostructures Induced by the Kirkendall Effect: The Basic Concept. *Nano Lett.* **2007,** *7*, 993-997.
31. Prins, R., On the structure of γ-Al_2O_3. *J. Catal.* **2020,** *392*, 336-346.
32. Quach, D. V.; Bonifacio, A. R.; Castro, R. H. R., Water adsorption and interface energetics of zinc aluminate spinel nanoparticles: Insights on humidity effects on nanopowder processing and catalysis. *J. Mater. Res.* **2013,** *28*, 2004-2011.
33. Zhou, R.-S.; Snyder, R. L., Structures and transformation mechanisms of the η, γ and θ transition aluminas. *Acta Crystallogr. Sect. B: Struct. Sci., Cryst. Eng. Mater.* **1991,** *47*, 617-630.
34. Fischer, P., Neutronenbeugungsuntersuchung der Strukturen von $MgAl_2O_4$- und $ZnAl_2O_4$-Spinellen, in Abhängigkeit

von der Vorgeschichte. *Z. Kristallogr. Cryst. Mater.* **1967,** *124*, 275-302.

35. MacKenzie, K.; Smith, M., Multinuclear Solid State NMR of Inorg. Mater. 2002. Pergamon Press, Oxford.

36. Kunath-Fandrei, G.; Bastow, T. J.; Hall, J. S.; Jaeger, C.; Smith, M. E., Quantification of Aluminum Coordinations in Amorphous Aluminas by Combined Central and Satellite Transition Magic Angle Spinning NMR Spectroscopy. *J. Phys. Chem.* **1995,** *99*, 15138-15141.

37. Samain, L.; Jaworski, A.; Edén, M.; Ladd, D. M.; Seo, D.-K.; Javier Garcia-Garcia, F.; Häussermann, U., Structural analysis of highly porous γ-Al_2O_3. *J. Solid State Chem.* **2014,** *217*, 1-8.

38. Ayoola, H. O.; House, S. D.; Bonifacio, C. S.; Kisslinger, K.; Saidi, W. A.; Yang, J. C., Evaluating the accuracy of common γ-Al_2O_3 structure models by selected area electron diffraction from high-quality crystalline γ-Al_2O_3. *Acta Mater.* **2020,** *182*, 257-266.

39. Lee, M. H.; Cheng, C.-F.; Heine, V.; Klinowski, J., Distribution of tetrahedral and octahedral A1 sites in gamma alumina. *Chem. Phys. Lett.* **1997,** *265*, 673-676.

40. Sakurai, S.; Sasaki, S.; Okube, M.; Ohara, H.; Toyoda, T., Cation distribution and valence state in Mn–Zn ferrite examined by synchrotron X-rays. *Physica B: Condens. Matter* **2008,** *403*, 3589-3595.

41. Naeem, M. A.; Burueva, D. B.; Abdala, P. M.; Bushkov, N. S.; Stoian, D.; Bukhtiyarov, A. V.; Prosvirin, I. P.; Bukhtiyarov, V. I.; Kovtunov, K. V.; Koptyug, I. V.; Fedorov, A.; Müller, C. R., Deciphering the Nature of Ru Sites in Reductively Exsolved Oxides with Electronic and Geometric Metal–Support Interactions. *J. Phys. Chem. C* **2020,** *124*, 25299-25307.

42. Berndt, H.; Lietz, G.; Lücke, B.; Völter, J., Zinc promoted H-ZSM-5 catalysts for conversion of propane to aromatics I. Acidity and activity. *Appl. Catal. A-Gen.* **1996,** *146*, 351-363.

43. Baddour-Hadjean, R.; Pereira-Ramos, J.-P., Raman Microspectrometry Applied to the Study of Electrode Materials for Lithium Batteries. *Chem. Rev.* **2010,** *110*, 1278-1319.

44. Ferrari, A. C.; Meyer, J. C.; Scardaci, V.; Casiraghi, C.; Lazzeri, M.; Mauri, F.; Piscanec, S.; Jiang, D.; Novoselov, K. S.; Roth, S.; Geim, A. K., Raman Spectrum of Graphene and Graphene Layers. *Phys. Rev. Lett.* **2006,** *97*, 187401.

45. Ferrari, A. C.; Basko, D. M., Raman spectroscopy as a versatile tool for studying the properties of graphene. *Nat. Nanotechnol.* **2013,** *8*, 235-246.

46. Mallet-Ladeira, P.; Puech, P.; Toulouse, C.; Cazayous, M.; Ratel-Ramond, N.; Weisbecker, P.; Vignoles, G. L.; Monthioux, M., A Raman study to obtain crystallite size of carbon materials: A better alternative to the Tuinstra–Koenig law. *Carbon* **2014,** *80*, 629-639.

47. Wang, P.; Tanabe, E.; Ito, K.; Jia, J.; Morioka, H.; Shishido, T.; Takehira, K., Filamentous carbon prepared by the catalytic pyrolysis of CH_4 on Ni/SiO_2. *Appl. Catal. A-Gen.* **2002,** *231*, 35-44.

48. Guo, J.; Lou, H.; Zheng, X., The deposition of coke from methane on a $Ni/MgAl_2O_4$ catalyst. *Carbon* **2007,** *45*, 1314-1321.

49. Naeem, M. A.; Abdala, P. M.; Armutlulu, A.; Kim, S. M.; Fedorov, A.; Müller, C. R., Exsolution of Metallic Ru Nanoparticles from Defective, Fluorite-Type Solid Solutions $Sm_2RuxCe_{2-x}O_7$ To Impart Stability on Dry Reforming Catalysts. *ACS Catal.* **2020,** *10*, 1923-1937.

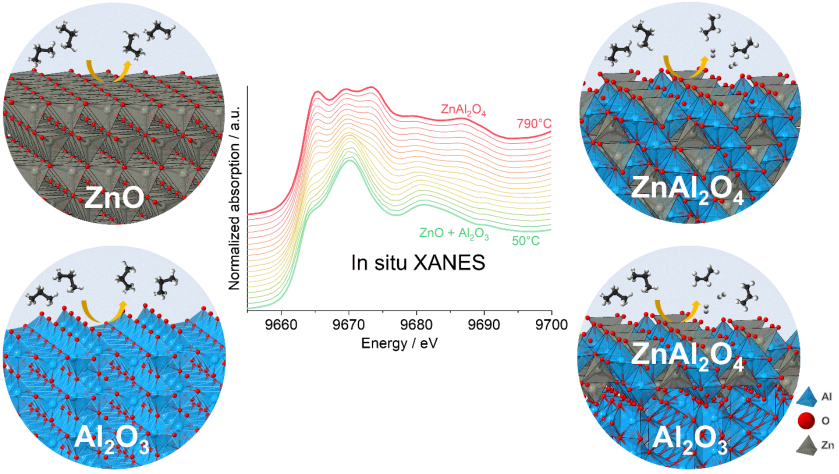
ZnO
Al$_2$O$_3$
Normalized absorption / a.u.
ZnAl$_2$O$_4$
790°C
ZnO + Al$_2$O$_3$
50°C
In situ XANES
9660
9670
9680
9690
9700
Energy / eV
ZnAl$_2$O$_4$
ZnAl$_2$O$_4$
Al$_2$O$_3$
Al
O
Zn

Supporting Information

Materials synthesis and basic characterization

Bulk-$ZnAl_2O_4$ was synthesized according to a literature method that is reproduced below for convenience.[1] $Zn(NO_3)_2{\cdot}6H_2O$ (1.488 g, 5 mmol) and $AlCl_3{\cdot}6H_2O$ (2.414 g, 10 mmol) were dissolved in deionized (DI) water to obtain a solution with a total cation concentration of 15 mmol L^{-1}. Citric acid (4.728 g, 24.6 mmol) was added to the transparent solution as a chelating agent, followed by dissolution of 20 g (111 mmol) of glucose. Subsequently acrylamide (9.596 g, 78.7 mmol) and N, N'-methylene-bisacrylamide (1.919 g, 12.5 mmol) monomers were added to the solution. The temperature of the solution was increased to 90 °C under continuous stirring in an oil bath and kept for 24 h to form a transparent gel. The gel was dried for 24 h and calcined at 1200 °C (4 °C min^{-1}) for 4 h under static air.

For the synthesis of $Zn_xAl_yO_4$ nanoparticles with varying Zn/Al ratios, the following respective amounts were used: 8.76 g (1.5 mmol) and 7.114 g (1.2 mmol) PEG, 1.813 g (6.1 mmol) and 4.409 g (14.8 mmol) $Zn(NO_3)_2{\cdot}6H_2O$, 11.432 g (30.5 mmol) and 5.559 g (14.8 mmol) $Al(NO_3)_3{\cdot}9H_2O$, respectively (see the main text Table 2, the determined Zn/Al ratios by ICP). Bulk $ZnAl_2O_4$ was synthesized using a gel-combustion technique and $AlCl_3{\cdot}6H_2O$ and $Zn(NO_3)_2{\cdot}6H_2O$ as precursors. Calcination was performed at 1200 °C for 4 h in a muffle furnace under static air using a 4 °C min^{-1} temperature ramp rate to ensure high crystallinity. For the TEM-EDX mapping of ALD 30ZnO/SiO_2, spherical silica (≥99%, Glantreo, 35 m^2 g^{-1}) was used instead of Aerosil 300 following the exact procedure reported in the main text. Catalytic tests of the $Zn_xAl_yO_4$ NPs were done in similar setup as for ZnO/Al_2O_3 using a Clarus-580 PerkinElmer gas chromatograph equipped with a methanizer. All carbon based products were separated by a HP Plot Q Restek column and analysed by a flame ionization detector (FID). H_2, N_2, and O_2 were separated by a ShinCarbon ST 80/100 Restek column and analysed by a thermal conductivity detector (TCD). Inductively Coupled Plasma Atomic Emission Spectroscopy (ICP-AES) were performed in Mikroanalytisches Labor Pascher, Remagen, Germany.

Equations

As thermal cracking also contributes to the observed conversions at 600 °C,[2] background thermal cracking was subtracted from the observed conversions to calculate the specific activity (mmol C_3H_6 mol Zn^{-1} h^{-1}), similar to what is reported elsewhere.[3]

$$\text{Specific activity} = \frac{F\left(\text{ml h}^{-1}\right)\times\left(y_{C3H6}\text{-BKG } y_{C3H6}\right)\times\text{Zn Mw (g mol}^{-1})}{24450\left(\text{ml mol}^{-1}\right)\times\ \text{catalyst weight (g)}\ \times\text{Zn weight fraction}}$$

where F is the total flow in ml h^{-1}; 24450 is the molar volume of a gas at room temperature and atmospheric pressure; y_{C3H6} is the mole fraction of C_3H_6 in the products when the catalyst is present; BKG y_{C3H6} (Background y_{C3H6}) is the mole fraction of C_3H_6 in the products without catalyst, i.e., when the reactor was loaded only with SiC.

In situ XAS-XRD under PDH conditions

In situ XAS and XRD measurements were performed at the Swiss-Norwegian beamlines (SNBL, BM31) at the European Synchrotron Radiation Facility (ESRF), Grenoble, France. The material was placed between two quartz wool plugs in a quartz capillary reactor cell (1.5 mm outer diameter, 0.1 mm wall thickness) that was glued to the stainless steel reactor and tested for leaks before the measurements. The middle of the quartz capillary was adjusted in the middle of the blower and fixed during all experiments. The temperature of the reaction zone was calibrated using a K type thermocouple placed in the middle of the quartz capillary under 10 mL min^{-1} of N_2 ; the gas flow rates were controlled using Bronkhorst mass flow controllers (MFC). Schematics of the experimental setup and the methodology used are given elsewhere.[4] The minimum temperature was always 50 °C and a temperature ramp rate of 10 °C min^{-1} was used. For the in situ calcination of as deposited 50ZnO/Al_2O_3, the temperature was increased from 50 °C to 650 °C and every 100 °C XAS and XRD spectra were recorded, then the temperature was further increased to 700, 750, and 790 °C and further XRD and XAS data were recorded. For the in situ propane dehydrogenation reaction, the specimen was heated (10 °C min^{-1}) up to 600 °C under He (10 mL min^{-1}) and after the temperature was stabilized the gas flow was switched to 10 mol.% C_3H_8 in He (10 mL min^{-1}). After one reaction cycle (ca. 90 min) one regeneration cycle (ca. 20 min) was performed at 650 °C using 20 mol.% O_2 in He that was followed by another reaction cycle (ca. 90 min) at 600 °C. During the reaction XAS-XRD data were being recorded every ca. 8 minutes. After the second cycle of PDH, the catalyst was cooled down under He (10 mL min^{-1}) and the data was recorded at 50 °C.

EXAFS analysis

Extended X-ray absorption fine structure (EXAFS) data were treated and analysed using the Demeter program package.[5] The theoretical model used for the EXAFS fitting was generated from the $ZnAl_2O_4$ spinel structure. Fittings were performed in R-space using R ranges between 1.3 - 3.4 Å and k= 3-12 $Å^{-1}$ (k^3-weight). The amplitude reduction factor, S_0=0.8 was determined from a bulk $ZnAl_2O_4$ material measured at the same conditions. Debye Waller-factors σ^2 were first refined and then fixed to the best values for all the studied materials in order to avoid high correlation between σ^2 and coordination numbers (CN). Coordination numbers, interatomic distances and energy shift were variables during the fitting.

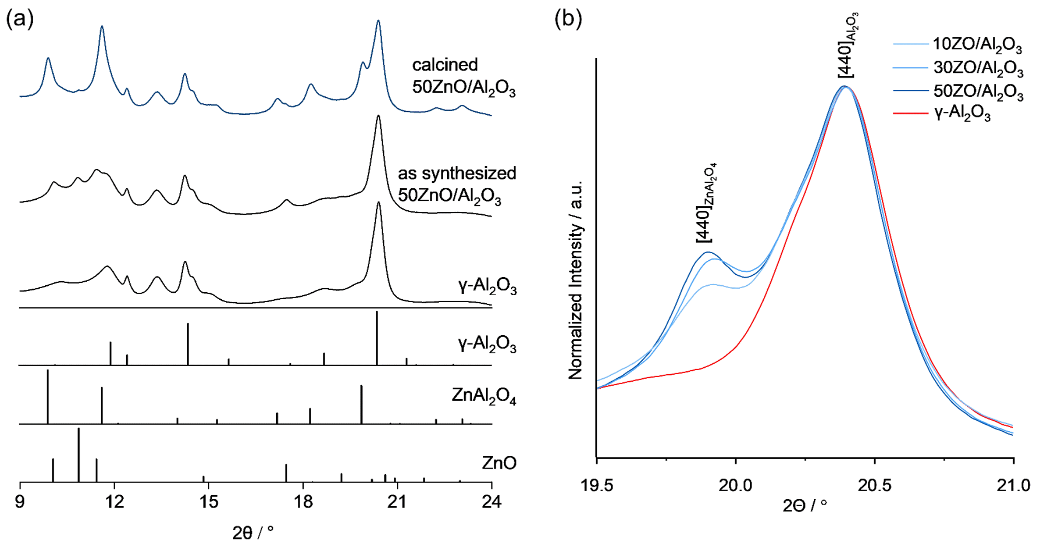

Figure S5. (a) XRD of as synthesized and calcined 50ZnO/Al$_2$O$_3$; (b) 440 XRD (λ=0.493 Å) peaks of γ-Al$_2$O$_3$ and ZnAl$_2$O$_4$ in calcined ALD ZnO/Al$_2$O$_3$ materials.

The ratio of the 440 peak of ZnAl$_2$O$_4$ to that of γ-Al$_2$O$_3$ $I_{(ZnAl2O4)}$: $I_{(Al2O3)}$ was 0.30, 0.34, and 0.40 for 10ZnO/Al$_2$O$_3$, 30ZnO/Al$_2$O$_3$, and 50ZnO/Al$_2$O$_3$, respectively.

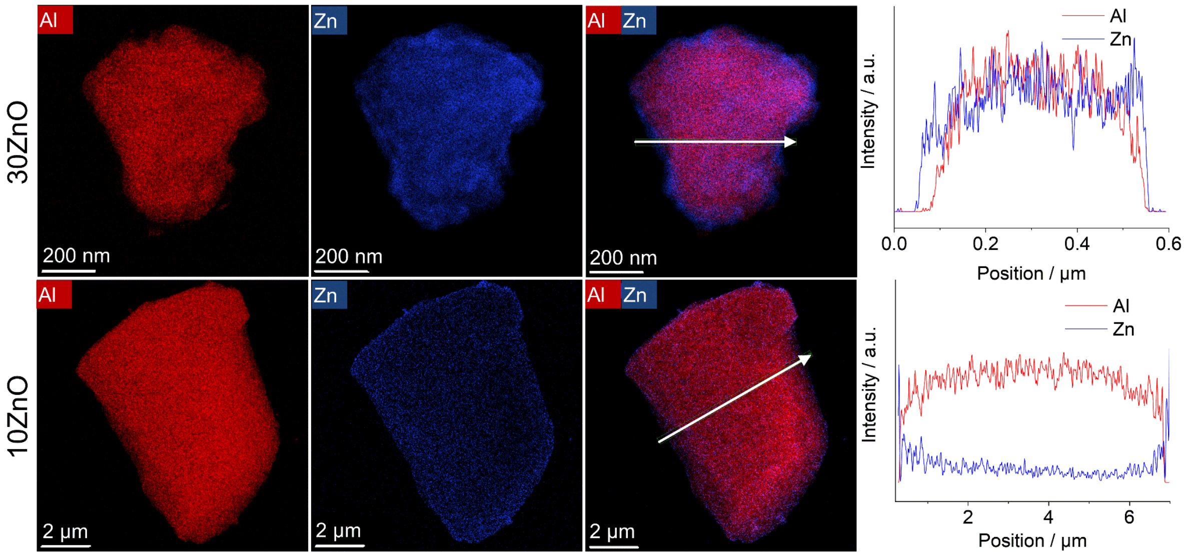

Figure S6. TEM-EDX and line mapping of calcined 10ZnO/Al$_2$O$_3$ and 30ZnO/Al$_2$O$_3$.

Both materials were handled in air.

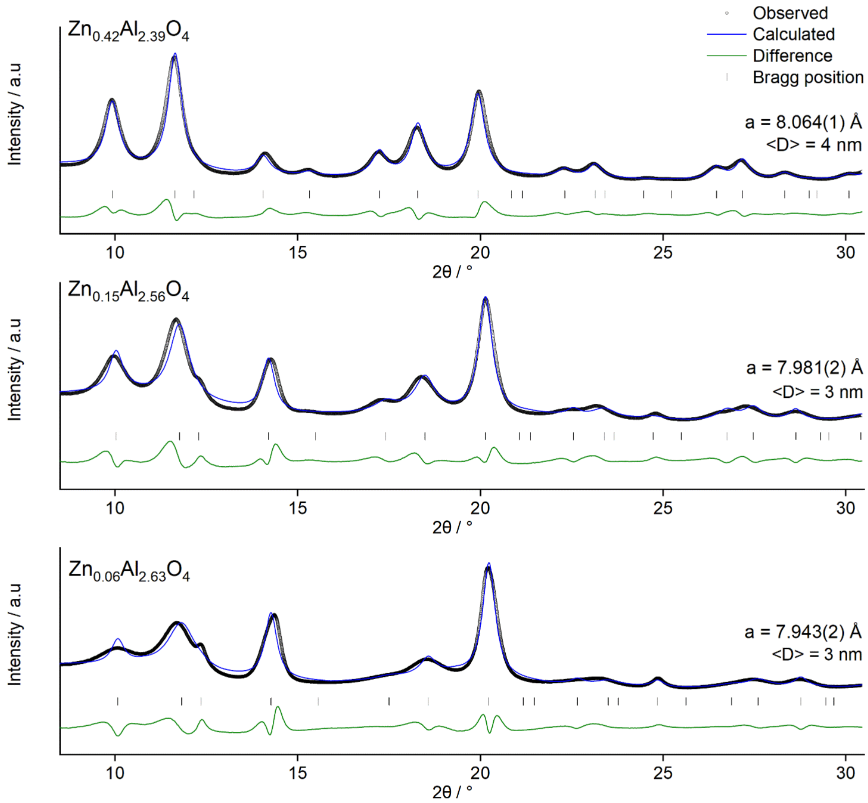

Figure S7. Le Bail fits of the synchrotron based XRD (λ=0.493 Å) of $Zn_xAl_yO_4$ NPs.[6]

<D> stand for mean crystallite diameter and a is the unit cell parameter (refined values during the fittings), space group *Fd*3*m*.

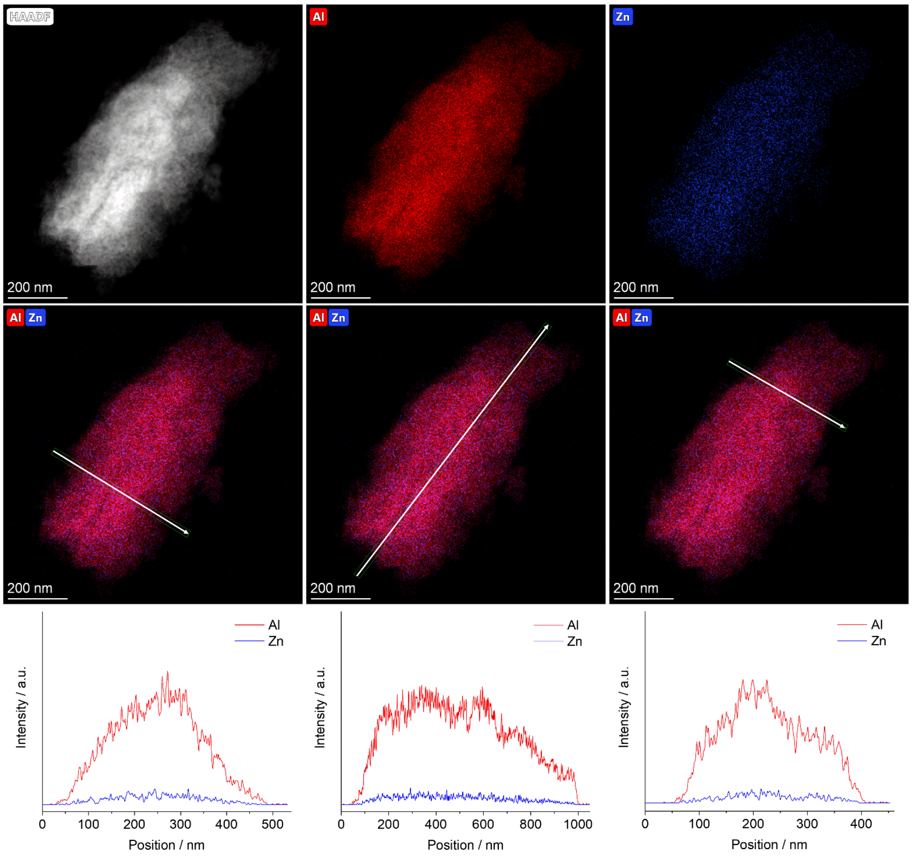

Figure S8. TEM-EDX and line mapping of as synthesized $Zn_{0.15}Al_{2.56}O_4$ NPs handled in air.

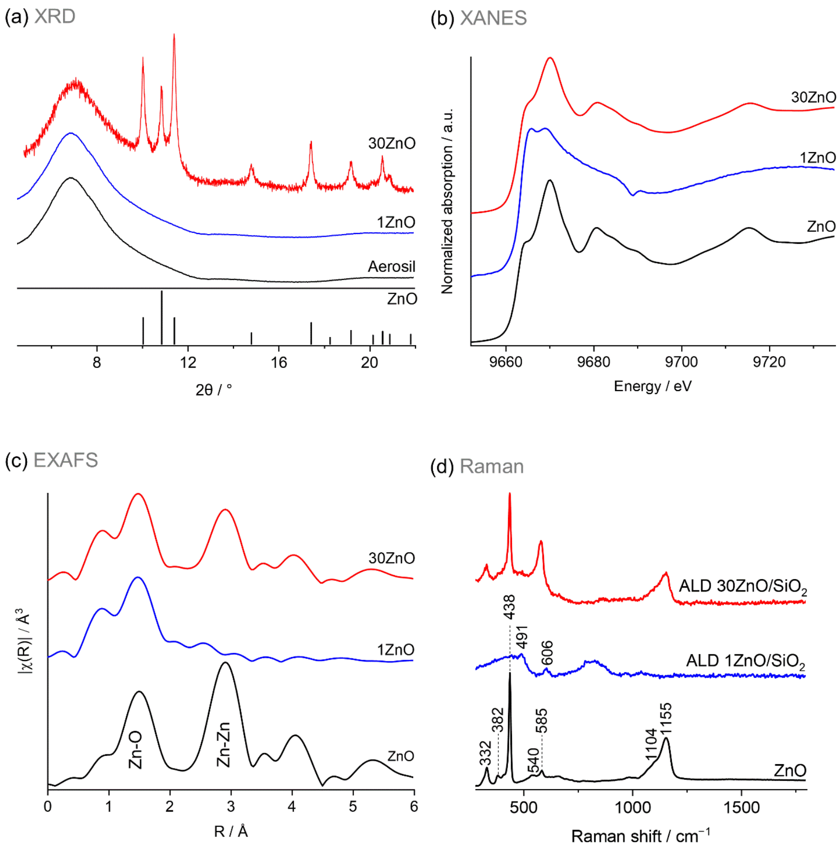

Figure S9. (a) XRD (λ=0.493 Å); (b) XANES; (c) EXAFS; (d) Raman spectroscopy of ALD ZnO/SiO$_2$.

All measurement were performed in air.

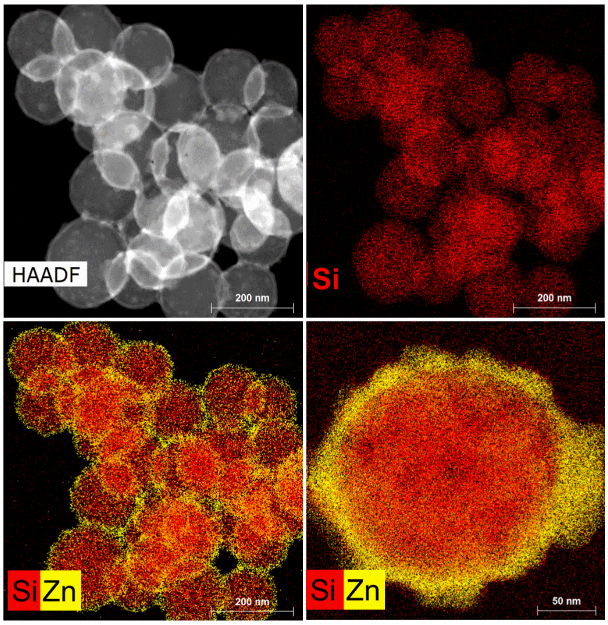

Figure S10. TEM EDX mapping of 50ZnO/SiO$_2$.

Spherical silica was used instead of Aerosil 300.

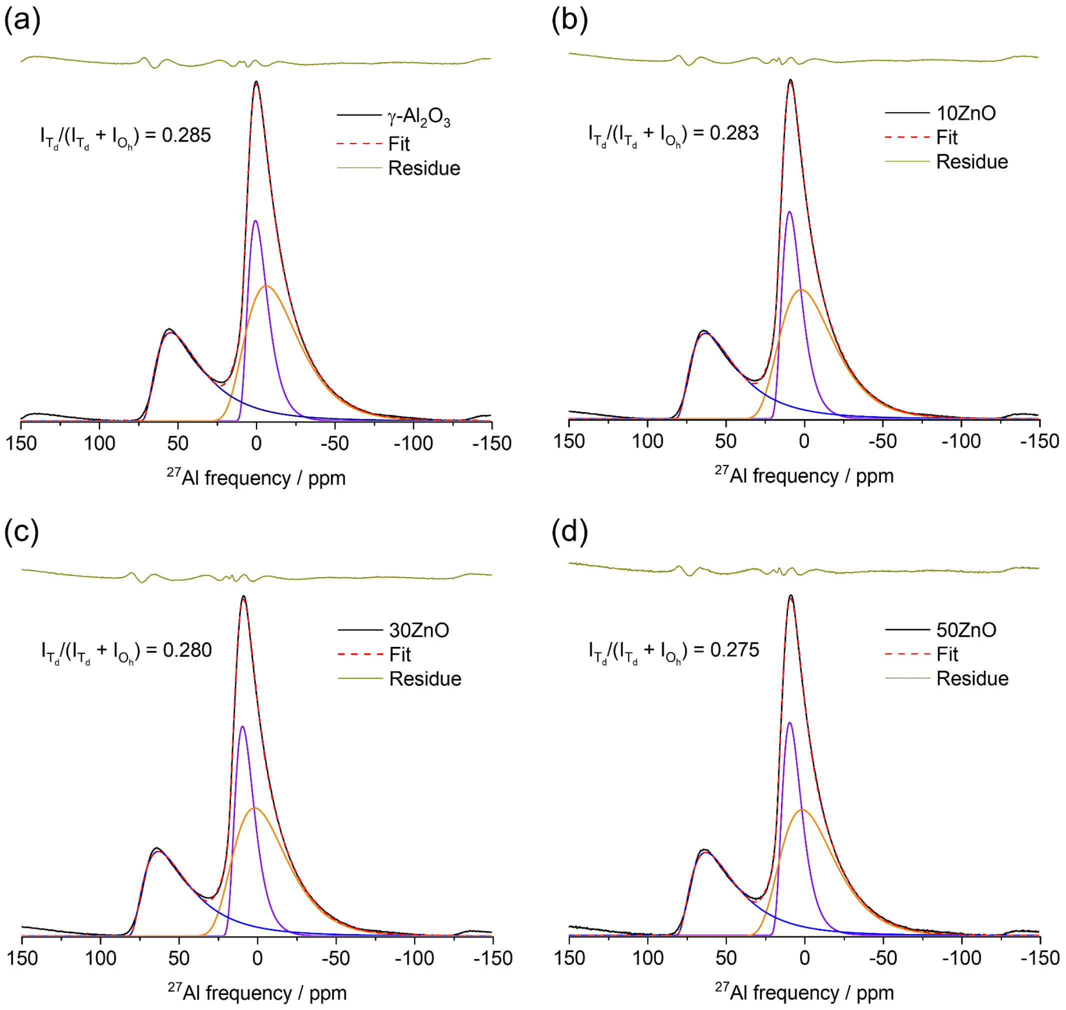

Figure S11. Peak fitting of ^{27}Al MAS NMR spectrum of γ-Al_2O_3 and ALD ZnO/Al_2O_3 to calculate the peak ratios.

The peaks were fitted using asymmetric Lognormal functions. The peaks were fitted in a way that gives the best estimation of the areas and do not carry a physical meaning.

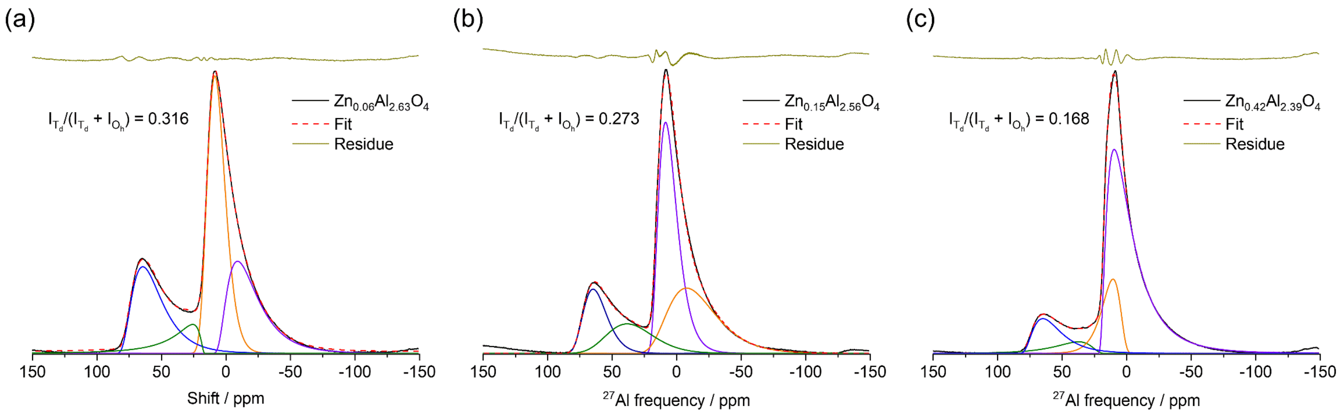

Figure S12. Peak fitting of ^{27}Al MAS NMR spectra of $Zn_xAl_yO_4$ NPs to calculate the peak ratios.

The peaks were fitted using asymmetric Lognormal functions. The peaks were fitted in a way that gives the best estimation of the areas and do not carry a physical meaning.

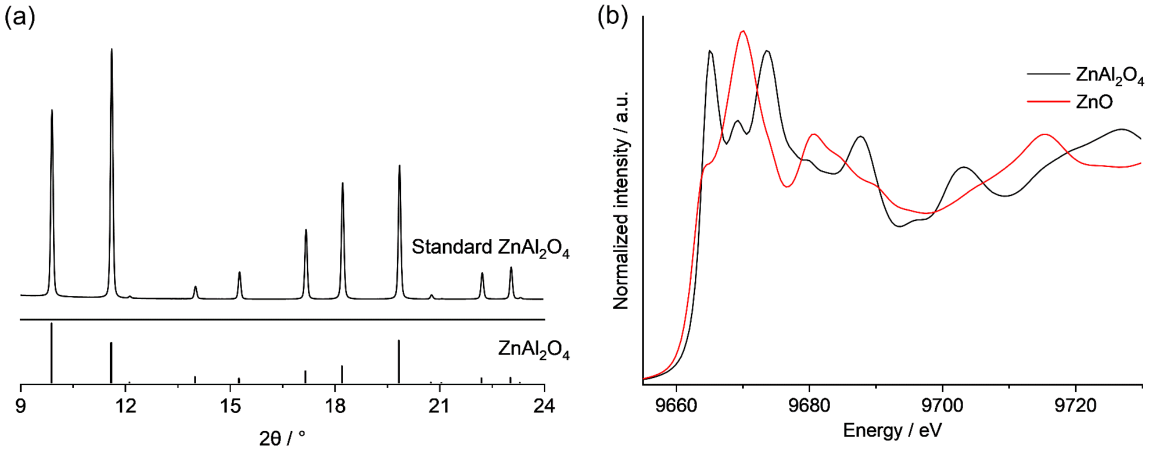

Figure S13. (a) XRD (λ=0.493 Å) pattern of standard bulk-$ZnAl_2O_4$ together with a simulated pattern according to ICSD data base (ICSD collection code = 26849); (b) XANES of wurtzite ZnO and bulk-$ZnAl_2O_4$

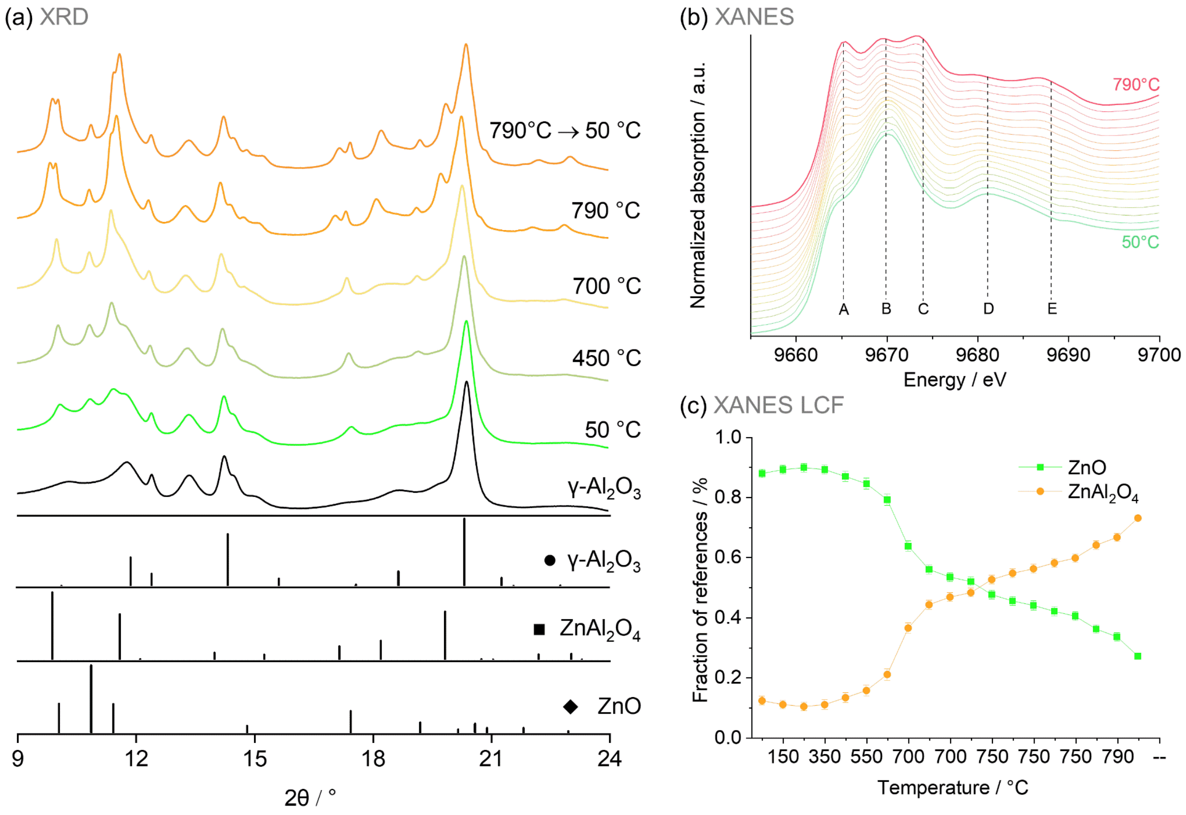

Figure S14 In situ (a) XRD (λ=0.493 Å); (b) XANES and (c) linear combination fitting (LCF) analysis of the XANES data, during heating in 20% O_2 in He of 50ZnO/Al_2O_3 from room temperature up to 790 °C.

Legends show the temperature at which the measurement was performed.

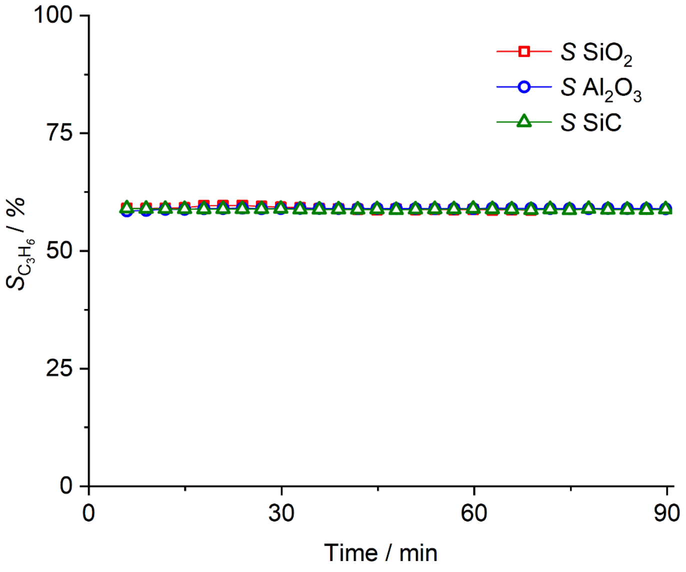

Figure S15. C_3H_6 selectivity of the bare supports and SiC in PDH.

100 mg of Al_2O_3 or SiO_2 mixed with 200 mg of SiC as well as 200 mg bare SiC were tested under a total flow of 21 ml min^{-1} of 10% C_3H_8 balanced in N_2 at 600 °C.

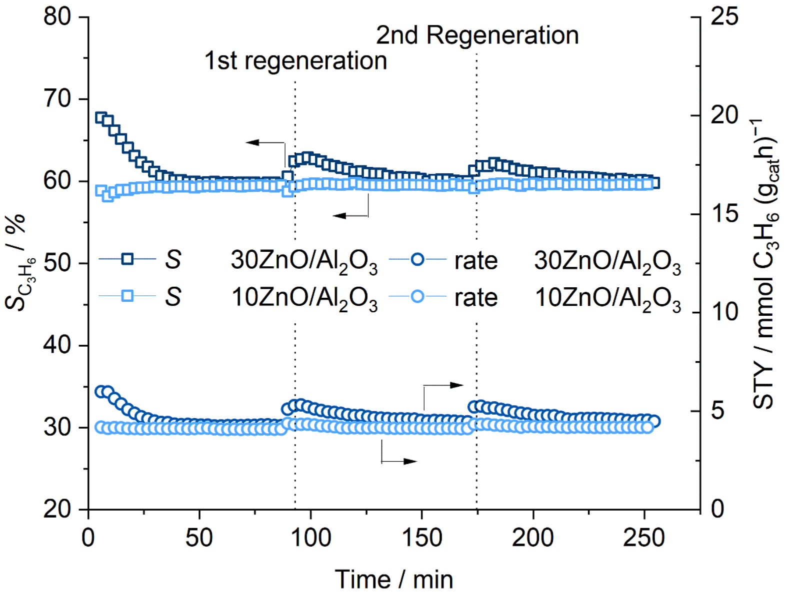

Figure S16. Cyclic catalytic activity of ALD 30ZnO/Al_2O_3 and 10ZnO/Al_2O_3.

Materials were tested under a total flow of 21 ml min^{-1} of 10% C_3H_8 balanced in N_2 at 600 °C, regeneration was carried out under synthetic air at 650 °C for 20 min. Catalysts were purged for 10 min using 21 ml min^{-1} pure N_2 after each regeneration cycle.

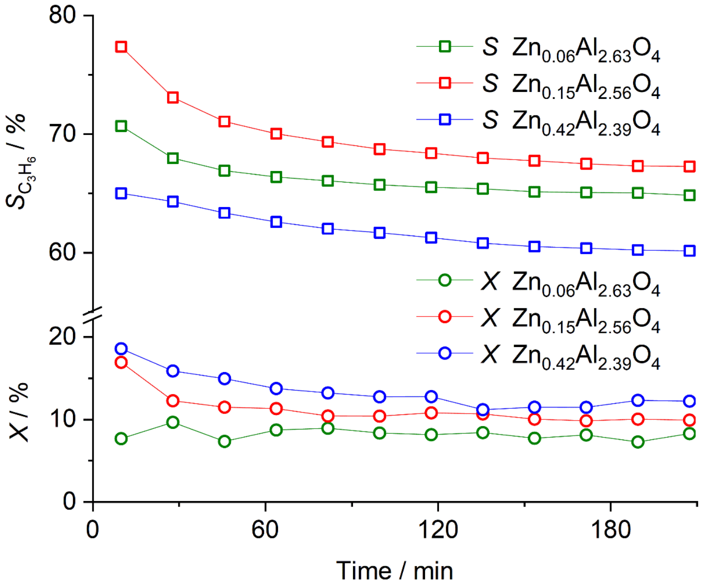

Figure S17. Catalytic performance of $Zn_xAl_yO_4$ NPs with time on stream (TOS).

Materials were tested under a total flow of 21 ml min^{-1} of 10% C_3H_8 balanced in N_2 at 600 °C.

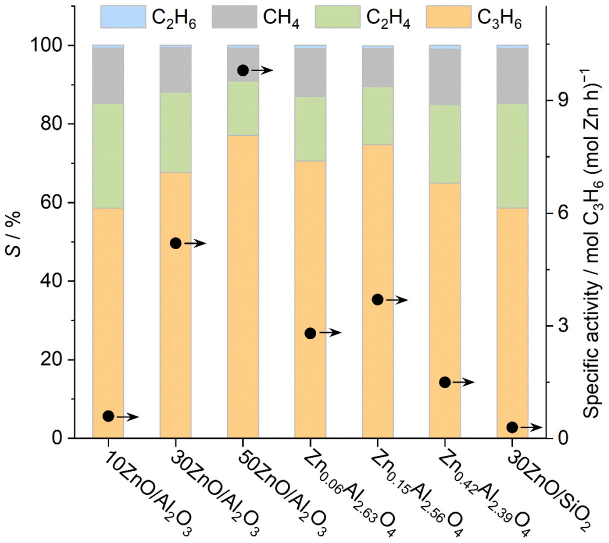

Figure S18. Initial specific activity (mol C_3H_6 (mol$_{Zn}$ h)$^{-1}$) of the studied materials under PDH conditions.

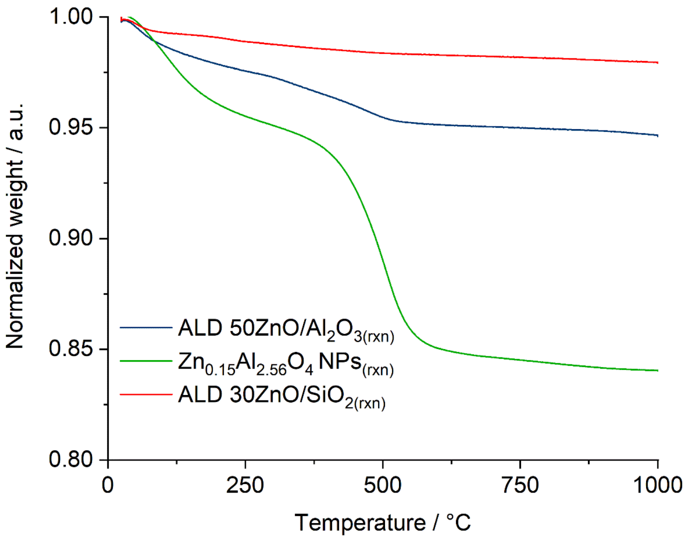

Figure S19. TPO experiment in a TGA using reacted catalysts (3 cycles).

Materials were tested under a total flow of 21 ml min^{-1}, 10 mol.% C_3H_8 in N_2, at 600 °C for three 90 min cycles followed by two 30 min regeneration cycles in between using synthetic air at 650 °C. Temperature programmed oxidation (TPO) was carried out, on the reacted catalysts after the 3rd reaction cycle, using 30 ml min^{-1} synthetic air and a 10 °C min^{-1} temperature ramp rate up to 1000 °C. See Table S2 for the quantitative results.

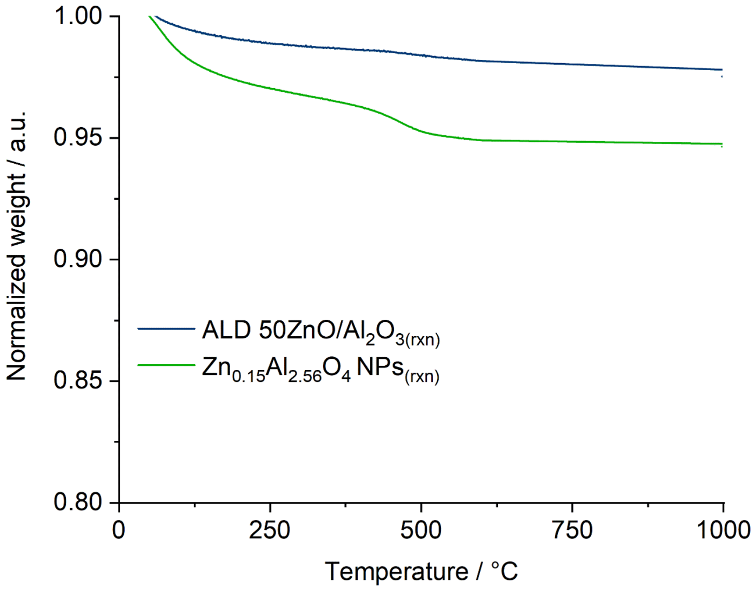

Figure S20. TPO experiments in a TGA using reacted catalysts (1 cycle).

The amount of the coke per unit surface area of the catalyst was calculated as 0.2 and 0.25 mg m^{-2} for 50ZnO/Al_2O_3 and $Zn_{0.15}Al_{2.56}O_4$, respectively (Table S2). Materials were reacted under a total flow of 21 ml min^{-1}, 10 mol.% C_3H_8 in N_2, at 600 °C for one 90 min cycle. Temperature programmed oxidation (TPO) was carried out using the reacted catalysts after the first reaction cycle, using 30 ml min^{-1} synthetic air and a 10 °C min^{-1} temperature ramp rate up to 1000 °C.

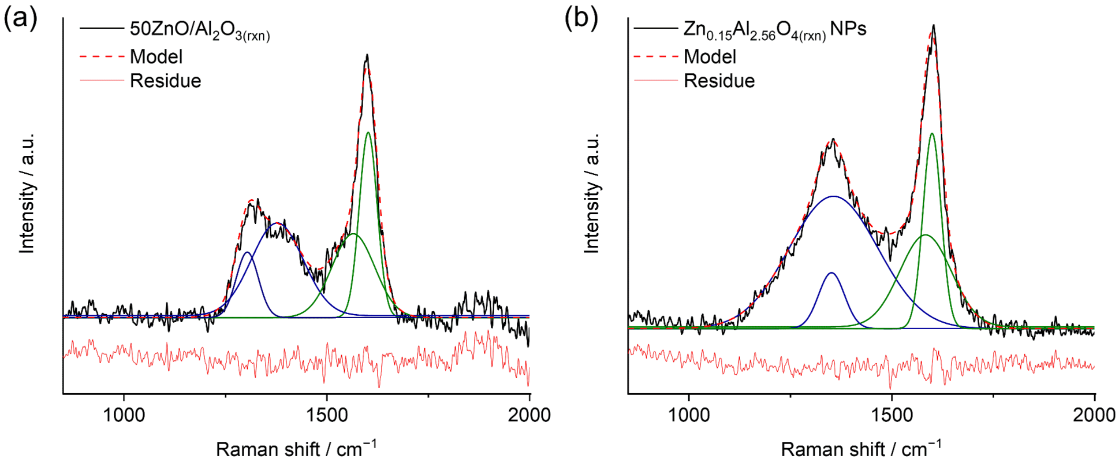

Figure S21. Raman spectra of ALD $50ZnO/Al_2O_3$ after the first cycle of PDH (90 min).

rxn indicates the catalyst after 90 min TOS (600 °C, 10 mol.% C_3H_8 in N_2). I_D/I_G equals to 0.91 and 1.59 for ALD $50ZnO/Al_2O_3$ and $Zn_{0.15}Al_{2.56}O_4$ NPs, respectively (Table S2). The peaks were fitted using Gaussian and Lognormal functions.

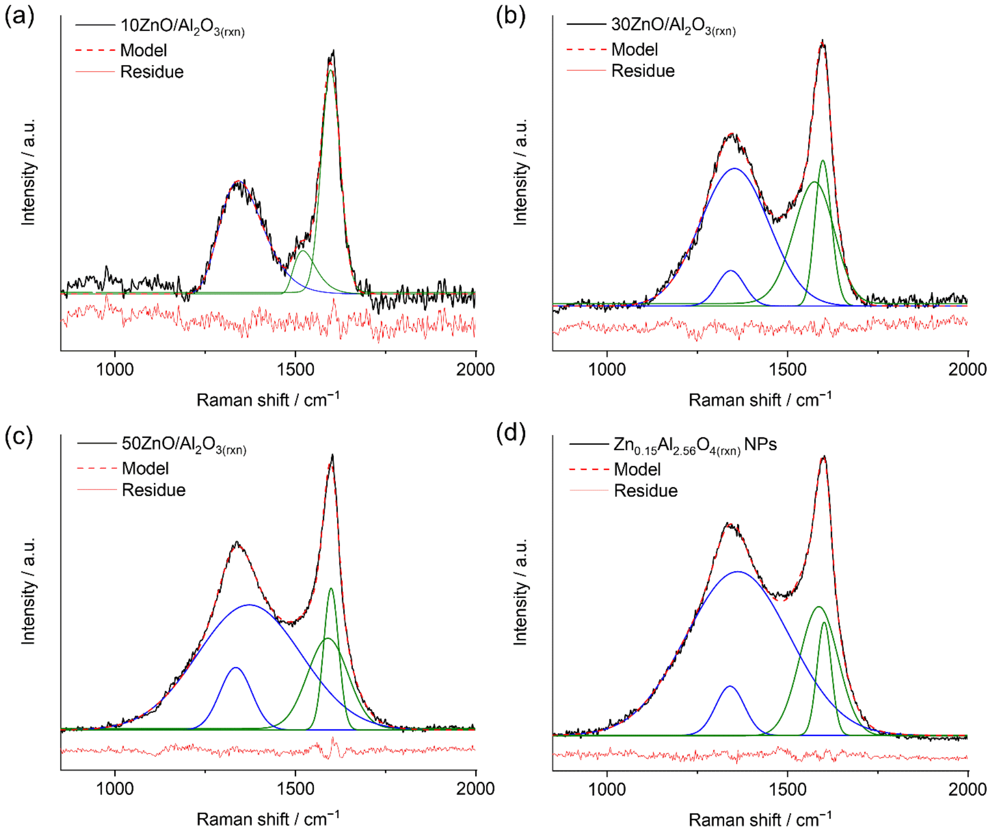

Figure S22. Raman spectra of reacted ALD ZnO/Al_2O_3 and $Zn_{0.15}Al_{2.56}O_4$ NPs after 3 cycles of PDH reaction (270 min).

rxn indicates the catalyst after 270 min TOS (600 °C, 10 mol.% C_3H_8 in N_2) including two regeneration cycles (21 ml min^{-1} air at 650 °C for 20 min). Each cycle lasted 90 minutes of TOS. I_D/I_G equals to 0.95, 1.42, and 2.06 for ALD 10, 30, and $50ZnO/Al_2O_3$, respectively, and it equalled to 2.79 for $Zn_{0.15}Al_{2.56}O_4$ NPs (Table S2). The peaks were fitted using Gaussian and Lognormal functions.

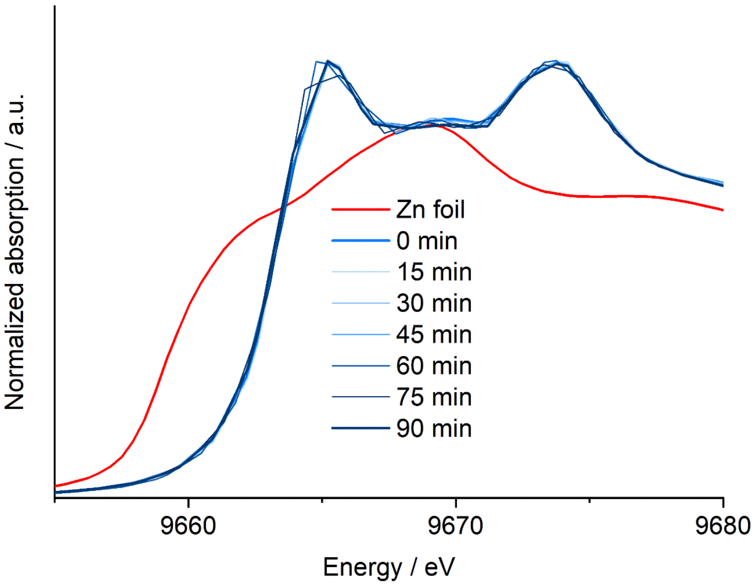

Figure S23. In situ XANES spectra of 50ZnO/Al₂O₃ during PDH reaction: 600 °C, 10 mol.% C_3H_8 in He.

Legends show the TOS at which the measurement was performed.

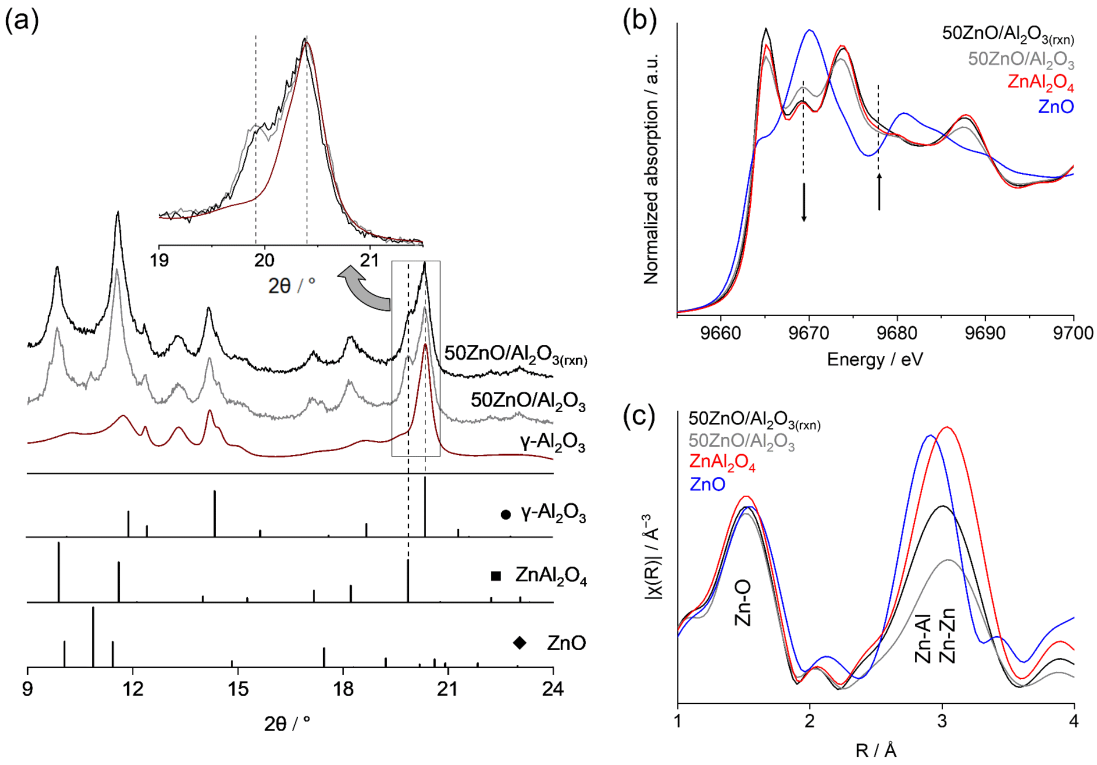

Figure S24. (a) XRD (λ=0.493 Å); (b) XANES; (c) EXAFS of 50ZnO/Al_2O_3 before and after the catalytic reaction (collected ex situ).

A total flow of 21 ml min^{-1} of 10% C_3H_8 balanced in N_2 was used. The used catalyst denoted by subscript (rxn) has been studied after 270 min TOS (600 °C, 10 mol.% C_3H_8 in N_2) including two regeneration cycles (21 ml min^{-1} air at 650 °C) after 90 minutes of TOS.

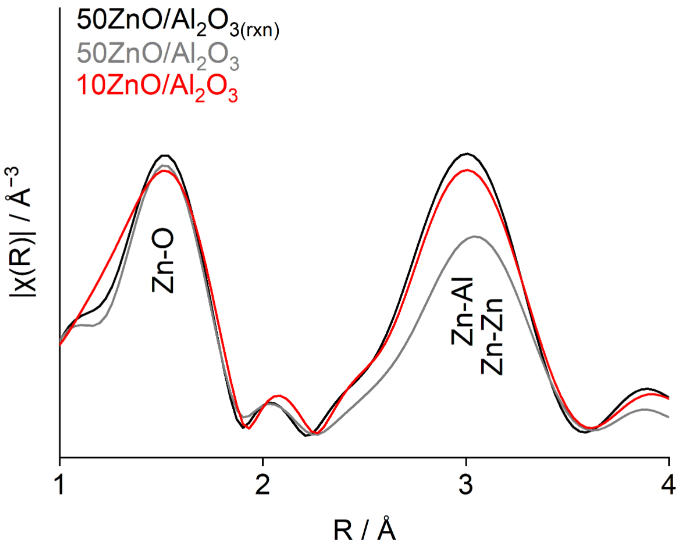

Figure S25. EXAFS-FT of 50ZnO/Al_2O_3 before and after 3 cycles of PDH reaction.

(rxn) indicates the catalyst after 270 min TOS (600 °C, 10 mol.% C_3H_8 in N_2) including two regeneration cycles (21 ml min^{-1} air at 650 °C for 20 min) after every 90 minutes of TOS.

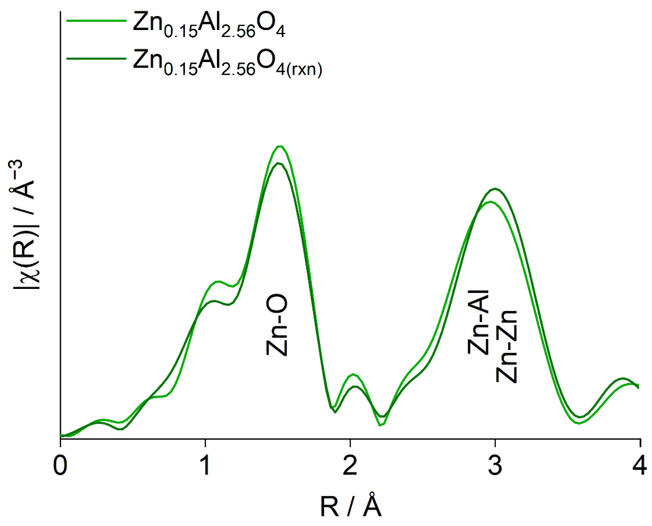

Figure S26. EXAFS-FT of $Zn_{0.15}Al_{2.56}O_4$ NPs before and after 3 cycles of PDH reaction.

rxn indicates the catalyst after 270 min TOS (600 °C, 10 mol.% C_3H_8 in N_2) including two regeneration cycles (21 ml min^{-1} air at 650 °C for 20 min) after every 90 minutes of TOS.

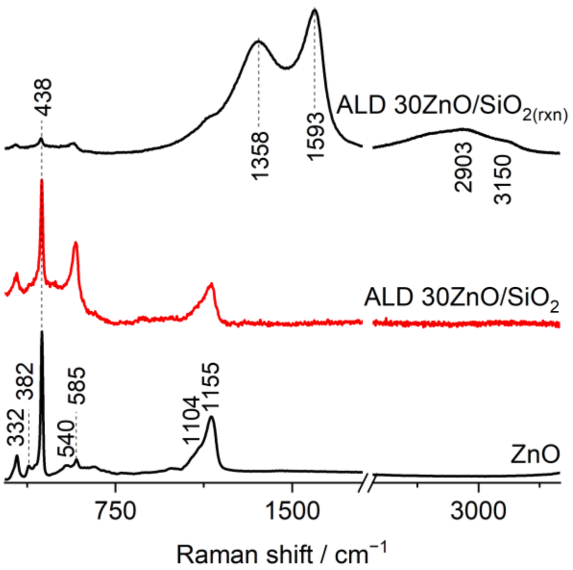

Figure S27. Raman spectra of ALD 30ZnO/SiO2 before and after the catalytic reaction. Material was reacted in a total flow of 21 ml min^{-1} of 10 mol.% C_3H_8 in N_2 at 600 °C for three 90 min cycles followed by two 30 min regeneration cycles in between using synthetic air at 650 °C.

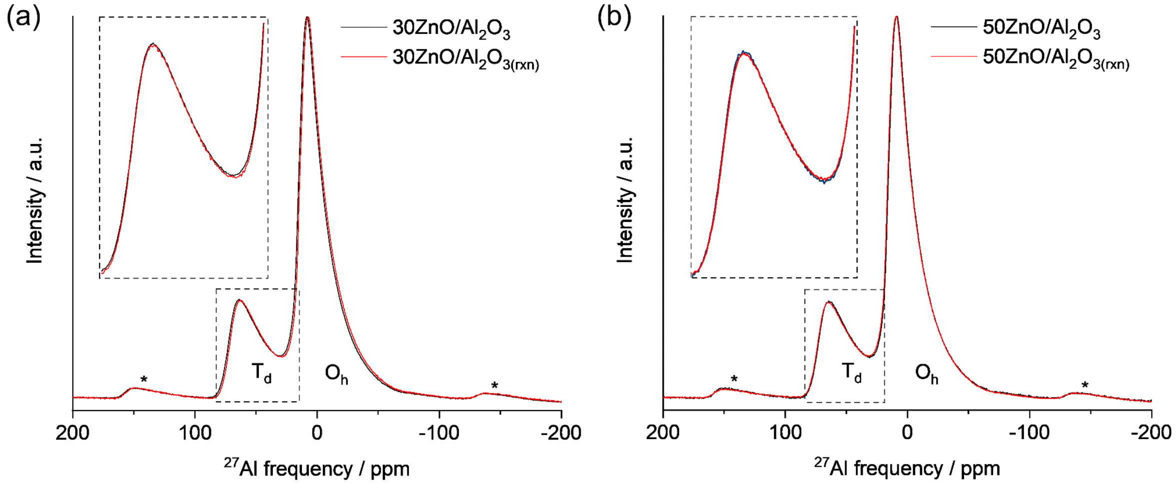

Figure S28. ^{27}Al MAS NMR of ALD 30 and 50ZnO/Al_2O_3 before and after the catalytic reaction. Sidebands are marked by asterisks. 15 kHz spinning rate was used. rxn indicates the catalyst after 270 min TOS (600 °C, 10 mol.% C_3H_8 in N_2); including two regeneration cycles every 90 minutes TOS (21 ml min^{-1} air flow at 650 °C).

Table S4. Structural parameters determined from EXAFS fitting of the Zn K-edge EXAFS data for ALD ZnO/Al$_2$O$_3$.

Material	Scattering Path	CN	σ^2	R / Å	E_0	R factor
10ZnO/Al$_2$O$_3$	Zn-O1	3.6(4)	0.003*	1.96(1)	5(1)	0.019
	Zn-Al	7(2)	0.004*	3.36(1)		
	Zn-O2	7**	0.004*	4.0*		
	Zn-Zn	3(1)	0.004*	3.54(2)		
30ZnO/Al$_2$O$_3$	Zn-O1	3.7(4)	0.003*	1.95(1)	4(1)	0.012
	Zn-Al	5(1)	0.004*	3.35(1)		
	Zn-O2	5**	0.004*	4.0*		
	Zn-Zn	3(1)	0.004*	3.53(2)		
50ZnO/Al$_2$O$_3$	Zn-O1	3.9(4)	0.003*	1.95(1)	3(1)	0.009
	Zn-Al	4(1)	0.004*	3.34(1)		
	Zn-O2	4**	0.004*	4.0*		
	Zn-Zn	4(1)	0.004*	3.53(2)		
50ZnO/Al$_2$O$_{3(rxn)}$	Zn-O1	4.0(4)	0.003*	0.003*	3(1)	0.014
	Zn-Al	6(1)	0.004*	0.004*		
	Zn-O2	6**	0.004*	0.004*		
	Zn-Zn	4(1)	0.004*	0.004*		
Zn$_{0.06}$Al$_{2.63}$O$_4$	Zn-O1	3.6(3)	0.003*	1.96(1)	3(1)	0.024
	Zn-Al	5(1)	0.004*	3.35(1)		
	Zn-O2	5**	0.004*	4.0*		
	Zn-Zn	2(1)	0.004*	3.52(2)		
Zn$_{0.15}$Al$_{2.56}$O$_4$	Zn-O1	4.0(4)	0.003*	1.94(1)	3(1)	0.016
	Zn-Al	6(1)	0.004*	3.33(1)		
	Zn-O2	6**	0.004*	4.0*		
	Zn-Zn	3(1)	0.004*	3.53(2)		
Zn$_{0.42}$Al$_{2.39}$O$_4$	Zn-O1	3.5(5)	0.003*	1.95(1)	3(1)	0.015
	Zn-Al	5(1)	0.004*	3.33(1)		
	Zn-O2	5**	0.004*	4.0*		
	Zn-Zn	3(1)	0.004*	3.52(2)		
Zn$_{0.15}$Al$_{2.56}$O$_{4(rxn)}$	Zn-O1	3.8(5)	0.003*	1.95(1)	3(1)	0.014
	Zn-Al	6(1)	0.004*	3.33(1)		
	Zn-O2	6**	0.004*	4.0*		
	Zn-Zn	3(1)	0.004*	3.52(2)		
ZnAl$_2$O$_4$-bulk	Zn-O	4*	0.003(1)	1.95(1)	6(1)	0.016
	Zn-Al	12*	0.003(1)	3.38(1)		
	Zn-O2	4*	0.004(1)	4.0*		
	Zn-Zn	4*	0.004(1)	3.55(2)		

*Fixed to the crystallographic values during the fitting.

**restrained CN $_{Zn\text{-}O2}$=CN$_{Zn\text{-}Al}$

The values in the parenthesis are standard deviations obtained during fitting. Subscript rxn indicates the materials after 270 min TOS (600 °C, 10 mol.% C_3H_8 in N_2); including two regeneration (21 ml min^{-1} air at 650 °C) cycles every 90 minutes TOS.

Table S2. Detailed catalytic results.

Catalyst	Time	X (%)	$y_{C3H6}/\Sigma y$	$y_{C2H6}/\Sigma y$	$y_{C2H4}/\Sigma y$	$y_{CH4}/\Sigma y$	STY_{C3} (mmol C_3H_6 g_{cat}^{-1} h^{-1})	STY_{C2-} (mmol C_2H_6 + C_2H_4 + CH_4 $gcat^{-1}$ h^{-1})
10ZnO/Al_2O_3	3	5.0	0.42	0.01	0.28	0.29	4.07	5.61
	6	4.6	0.42	0.01	0.28	0.29	4.12	5.80
	9	5.1	0.41	0.01	0.28	0.30	4.06	5.87
	12	5.3	0.41	0.01	0.28	0.30	4.10	5.82
	15	5.3	0.42	0.01	0.28	0.29	4.09	5.74
	18	5.5	0.42	0.01	0.28	0.29	4.06	5.69
	21	5.6	0.42	0.01	0.28	0.29	4.05	5.63
	24	5.7	0.42	0.01	0.28	0.29	4.04	5.60
	27	5.8	0.42	0.01	0.28	0.29	4.05	5.61
	30	5.7	0.42	0.01	0.28	0.29	4.06	5.60
	33	5.7	0.42	0.01	0.28	0.29	4.05	5.59
	36	5.9	0.42	0.01	0.28	0.29	4.04	5.60
	39	6.1	0.42	0.01	0.28	0.29	4.07	5.60
	42	6.0	0.42	0.01	0.28	0.29	4.05	5.58
	45	6.2	0.42	0.01	0.28	0.29	4.04	5.57
	48	6.3	0.42	0.01	0.28	0.29	4.05	5.61
	51	6.3	0.42	0.01	0.28	0.29	4.07	5.61
	54	6.3	0.42	0.01	0.28	0.29	4.08	5.61
	57	6.3	0.42	0.01	0.28	0.29	4.04	5.57
	60	6.1	0.42	0.01	0.28	0.29	4.02	5.51
	63	6.4	0.42	0.01	0.28	0.29	4.01	5.52
	66	6.3	0.42	0.01	0.28	0.29	4.03	5.54
	69	6.3	0.42	0.01	0.28	0.29	4.01	5.54
	72	6.2	0.42	0.01	0.28	0.29	4.03	5.54
	75	6.6	0.42	0.01	0.28	0.29	4.02	5.52
	78	6.4	0.42	0.01	0.28	0.29	4.03	5.52
	81	6.4	0.42	0.01	0.28	0.29	4.03	5.54
	84	6.4	0.42	0.01	0.28	0.29	4.02	5.54
	87	6.4	0.42	0.01	0.28	0.29	4.03	5.52
	90	6.1	0.42	0.01	0.28	0.29	4.06	5.54

Continued **Table S2.** Detailed catalytic results

Catalyst	Time	*X* (%)	$y_{C3H6}/\Sigma y$	$y_{C2H6}/\Sigma y$	$y_{C2H4}/\Sigma y$	$y_{CH4}/\Sigma y$	STY_{C3} (mmol C_3H_6 g_{cat}^{-1} h^{-1})	STY_{C2-} (mmol C_2H_6 + C_2H_4 + CH_4 $gcat^{-1}$ h^{-1})
30ZnO/Al_2O_3	3	11.4	0.49	0.01	0.24	0.27	5.28	5.46
	6	9.6	0.51	0.01	0.23	0.26	5.93	5.74
	9	9.1	0.50	0.01	0.23	0.26	5.91	5.81
	6	9.6	0.49	0.01	0.24	0.26	5.93	5.74
	12	8.8	0.48	0.01	0.25	0.27	5.58	5.78
	15	8.4	0.47	0.01	0.25	0.27	5.31	5.75
	18	8.3	0.46	0.01	0.26	0.28	5.02	5.68
	21	8.1	0.45	0.01	0.26	0.28	4.83	5.71
	24	7.9	0.44	0.01	0.27	0.28	4.66	5.69
	27	7.7	0.44	0.01	0.27	0.29	4.54	5.67
	30	7.7	0.43	0.01	0.27	0.29	4.44	5.68
	33	7.6	0.43	0.01	0.27	0.29	4.36	5.71
	36	7.7	0.43	0.01	0.27	0.29	4.36	5.74
	39	7.7	0.43	0.01	0.27	0.29	4.28	5.72
	42	7.5	0.43	0.01	0.28	0.29	4.25	5.69
	45	7.7	0.43	0.01	0.28	0.29	4.26	5.74
	48	7.6	0.42	0.01	0.28	0.29	4.24	5.71
	51	7.7	0.43	0.01	0.28	0.29	4.23	5.73
	54	7.6	0.43	0.01	0.28	0.29	4.23	5.71
	57	7.5	0.42	0.01	0.28	0.29	4.19	5.64
	60	7.6	0.43	0.01	0.28	0.29	4.19	5.67
	63	7.6	0.42	0.01	0.28	0.29	4.20	5.68
	66	7.6	0.43	0.01	0.28	0.29	4.21	5.71
	69	7.5	0.43	0.01	0.28	0.29	4.20	5.68
	72	7.7	0.43	0.01	0.28	0.29	4.22	5.70
	75	7.6	0.42	0.01	0.28	0.29	4.21	5.70
	78	7.6	0.43	0.01	0.28	0.29	4.24	5.77
	81	7.5	0.43	0.01	0.28	0.29	4.24	5.73
	84	7.4	0.42	0.01	0.28	0.29	4.21	5.69
	87	7.6	0.43	0.01	0.28	0.29	4.20	5.73
	90	7.6	0.49	0.01	0.24	0.27	4.21	5.67

Continued **Table S2.** Detailed catalytic results.

Catalyst	Time	*X* (%)	$y_{C3H6}/\Sigma y$	$y_{C2H6}/\Sigma y$	$y_{C2H4}/\Sigma y$	$y_{CH4}/\Sigma y$	STY_{C3} (mmol C_3H_6 g_{cat}^{-1} h^{-1})	STY_{C2-} (mmol C_2H_6 + C_2H_4 + CH_4 $gcat^{-1}$ h^{-1})
50ZnO/Al_2O_3	3	17.2	0.62	0.01	0.17	0.20	9.01	5.50
	6	14.4	0.61	0.01	0.18	0.21	8.75	5.65
	9	12.7	0.59	0.01	0.19	0.22	8.04	5.59
	12	11.9	0.57	0.01	0.20	0.22	7.41	5.55
	15	11.2	0.56	0.01	0.21	0.23	6.93	5.53
	18	10.5	0.54	0.01	0.21	0.24	6.38	5.46
	21	9.9	0.52	0.01	0.22	0.25	6.02	5.46
	24	9.5	0.51	0.01	0.23	0.25	5.71	5.45
	27	9.1	0.50	0.01	0.24	0.26	5.43	5.43
	30	8.9	0.49	0.01	0.24	0.26	5.24	5.50
	33	8.6	0.48	0.01	0.24	0.27	5.13	5.51
	36	8.5	0.48	0.01	0.25	0.27	4.96	5.48
	39	8.2	0.47	0.01	0.25	0.27	4.82	5.44
	42	8.1	0.46	0.01	0.25	0.27	4.72	5.45
	45	7.9	0.46	0.01	0.26	0.27	4.64	5.40
	48	7.8	0.46	0.01	0.26	0.28	4.58	5.41
	51	7.8	0.45	0.01	0.26	0.28	4.53	5.44
	54	7.8	0.45	0.01	0.26	0.28	4.50	5.44
	57	7.6	0.45	0.01	0.26	0.28	4.47	5.41
	60	7.6	0.45	0.01	0.26	0.28	4.41	5.39
	63	7.5	0.45	0.01	0.26	0.28	4.41	5.42
	66	7.4	0.45	0.01	0.26	0.28	4.38	5.41
	69	7.6	0.45	0.01	0.26	0.28	4.38	5.43
	72	7.5	0.44	0.01	0.27	0.28	4.36	5.44
	75	7.4	0.44	0.01	0.27	0.28	4.34	5.45
	78	7.4	0.44	0.01	0.27	0.28	4.31	5.42
	81	7.5	0.44	0.01	0.27	0.28	4.29	5.41
	84	7.4	0.44	0.01	0.27	0.28	4.28	5.37
	87	7.3	0.44	0.01	0.27	0.28	4.30	5.43
	90	7.5	0.44	0.01	0.27	0.28	4.28	5.43

Continued **Table S2.** Detailed catalytic results.

Catalyst	Time	*X* (%)	$y_{C3H6}/\Sigma y$	$y_{C2H6}/\Sigma y$	$y_{C2H4}/\Sigma y$	$y_{CH4}/\Sigma y$	STY_{C3} (mmol C_3H_6 g_{cat}^{-1} h^{-1})	STY_{C2-} (mmol C_2H_6 + C_2H_4 + CH_4 $gcat^{-1}$ h^{-1})
$Zn_{0.15}Al_{2.56}O_4$	3	16.7	0.59	0.01	0.17	0.23	8.00	5.59
	6	13.6	0.57	0.01	0.18	0.23	7.68	5.72
	9	12.6	0.56	0.01	0.19	0.23	7.41	5.71
	12	12.4	0.56	0.01	0.20	0.24	7.07	5.67
	15	12.4	0.55	0.01	0.20	0.24	6.83	5.59
	18	12.4	0.54	0.01	0.20	0.24	6.67	5.59
	21	12.4	0.54	0.01	0.21	0.25	6.44	5.53
	24	12.0	0.53	0.01	0.21	0.25	6.35	5.55
	27	11.9	0.53	0.01	0.21	0.25	6.22	5.54
	30	11.8	0.52	0.01	0.22	0.25	6.09	5.54
	33	11.6	0.52	0.01	0.22	0.25	6.05	5.55
	36	11.4	0.52	0.01	0.22	0.25	5.95	5.53
	39	11.4	0.52	0.01	0.22	0.25	5.91	5.55
	42	11.3	0.51	0.01	0.22	0.26	5.86	5.59
	45	11.3	0.51	0.01	0.22	0.26	5.80	5.55
	48	11.2	0.51	0.01	0.22	0.26	5.74	5.56
	51	11.3	0.51	0.01	0.23	0.26	5.72	5.59
	54	10.9	0.50	0.01	0.23	0.26	5.64	5.54
	57	11.1	0.50	0.01	0.23	0.26	5.56	5.53
	60	11.1	0.50	0.01	0.23	0.26	5.56	5.54
	63	11.0	0.50	0.01	0.23	0.26	5.53	5.56
	66	10.9	0.50	0.01	0.23	0.26	5.48	5.54
	69	11.1	0.50	0.01	0.23	0.26	5.48	5.59
	72	11.0	0.49	0.01	0.23	0.27	5.46	5.60
	75	10.8	0.49	0.01	0.23	0.27	5.42	5.56
	78	10.8	0.49	0.01	0.23	0.27	5.38	5.55
	81	10.8	0.49	0.01	0.23	0.27	5.35	5.56
	84	10.8	0.49	0.01	0.23	0.27	5.33	5.54
	87	10.7	0.49	0.01	0.23	0.27	5.30	5.53
	90	10.5	0.49	0.01	0.23	0.27	5.28	5.53

Table S3. Carbon deposition assessed by Raman spectroscopy and TGA data

Material	**I_D/I_G (Raman)**	**Coke wt.% (TGA)**	**Coke per SA* (mg_{carbon} m^{-2}) (TGA)**
$10ZnO/Al_2O_3$ (3rd cycle)	0.95	-	-
$30ZnO/Al_2O_3$ (3rd cycle)	1.42	-	-
$50ZnO/Al_2O_3$ (3rd cycle)	2.06	4.86	0.52
$Zn_{0.15}Al_{2.56}O_4$ (3rd cycle)	2.79	14.95	0.73
$50ZnO/Al_2O_3$ (1st cycle)	0.91	1.85	0.2
$Zn_{0.15}Al_{2.56}O_4$ (1st cycle)	1.59	5.12	0.25

SA stands for surface area of the catalyst

Table S4. ICP-OES results before and after the catalytic reaction for ZnO/Al_2O_3 and ZnO/SiO_2

ALD Material	Zn (wt. %)	Zn (wt. %)$_{(rxn)}$
$10ZnO/Al_2O_3$	1.2	1.2
$30ZnO/Al_2O_3$	2.4	2.2
$50ZnO/Al_2O_3$	3.3	3.1
$10ZnO/SiO_2$	2.2	2.2
$30ZnO/SiO_2$	7.7	7.4

References

1. Wang, S.-F.; Sun, G.-Z.; Fang, L.-M.; Lei, L.; Xiang, X.; Zu, X.-T., A comparative study of $ZnAl_2O_4$ nanoparticles synthesized from different aluminum salts for use as fluorescence materials. *Sci. Rep.* **2015,** *5*, 12849.
2. Bhasin, M. M.; McCain, J. H.; Vora, B. V.; Imai, T.; Pujadó, P. R., Dehydrogenation and oxydehydrogenation of paraffins to olefins. *Appl. Catal. A* **2001,** *221*, 397-419.
3. Hu, B.; Schweitzer, N. M.; Zhang, G.; Kraft, S. J.; Childers, D. J.; Lanci, M. P.; Miller, J. T.; Hock, A. S., Isolated FeII on Silica As a Selective Propane Dehydrogenation Catalyst. *ACS Catal.* **2015,** *5*, 3494-3503.
4. Tsoukalou, A.; Abdala, P. M.; Stoian, D.; Huang, X.; Willinger, M.-G.; Fedorov, A.; Müller, C. R., Structural Evolution and Dynamics of an In_2O_3 Catalyst for CO_2 Hydrogenation to Methanol: An Operando XAS-XRD and In Situ TEM Study. *J. Am. Chem. Soc.* **2019,** *141*, 13497-13505.
5. Ravel, B.; Newville, M., ATHENA, ARTEMIS, HEPHAESTUS: data analysis for X-ray absorption spectroscopy using IFEFFIT. *J. Synchrotron Rad.* **2005,** *12*, 537-541.
6. Le Bail, A., Whole powder pattern decomposition methods and applications: A retrospection. *Powder Diffr.* **2005,** *20*, 316-326.